ORIGINAL PAPER

Corundum-quartz metastability: the role of silicon diffusion in corundum

Dina S. Schultze[1] · Richard Wirth[2] · Bernd Wunder[2] · Max Wilke[3] · Anselm Loges[1,4] · Gerhard Franz[1]

Abstract

The synthesis of the Al_2SiO_5 polymorphs kyanite, sillimanite and andalusite in a pure Al_2O_3–SiO_2–H_2O (ASH) system has long been known to be impeded. In order to decipher individual aspects of the reaction: corundum + $SiO_2 aq$, which repeatedly fails to produce thermodynamically stable Al_2SiO_5, we conducted experiments within the stability fields of kyanite and sillimanite (500–800 °C; 0.2–1 GPa) with the aim of forming reaction coronas on corundum. Results showed that metastable corundum + quartz assemblages form persistently in pure ASH, even in Al_2SiO_5 seeded experiments, despite the presence of catalyzing fluid and evidence of fast reaction kinetics. Coronas on corundum spontaneously formed when additional components (Na, K, N, and Mg) were added to the experiment. In a similar experiment with baddeleyite (ZrO_2) instead of corundum in silica saturated water, a zircon corona formed readily. This implies that nucleation and growth of Al_2SiO_5 is obstructed under conditions of Al and Si saturation in aqueous fluid, while both corundum and quartz saturated aqueous fluid are willing participants in other reactions towards stable corona formation. Instead of Al_2SiO_5 precipitation, an unexpected fluid-aided silica diffusion process into corundum was documented. The latter included the formation of nanometer wide hydrous silicate layers along the basal plane of the corundum host, which enhanced the silica diffusion rate drastically, leading to silica supersaturation in the host mineral, and ultimately to precipitation of quartz inside corundum. We conclude that the natural metastable assemblage of quartz and corundum is not necessarily the result of dry or fluid absent conditions, given that the aqueous fluid in experiments does not promote Al_2SiO_5 formation, but rather seems to support the formation and preservation of a metastable assemblage.

Keywords Metastability · Corundum · Quartz · Diffusion · Nanolayers · Aluminium-silicates

✉ Dina S. Schultze
dina.schultze@web.de

1 Fachgebiet Angewandte Geochemie, Technische Universitat Berlin, Ernst-Reuter-Platz 1, 10587 Berlin, Germany

2 Deutsche GeoForschungsZentrum Potsdam, Telegrafenberg, 14473 Potsdam, Germany

3 Institut für Erd- und Umweltwissenschaften, Universität Potsdam, Karl-Liebknecht-Str. 24-25, 14476 Potsdam-Golm, Germany

4 Arbeitsbereich Mineralogie-Petrologie, Freie Universität Berlin, Malteserstr. 74-100, 12249 Berlin, Germany

Introduction

The system Al_2O_3-SiO_2-H_2O (ASH) is notorious for its apparent inconsistencies between studies on natural samples, experimental results, and thermodynamic predictions. This suggests that there are important factors controlling the reaction behavior of this system, which are not understood at this point.

Despite suggestions that corundum + quartz might be a stable assemblage (Anovitz et al. 1993; Guiraud et al. 1996; Shaw and Arima 1998), thermodynamic data unequivocally determine the aluminium silicates (Al_2SiO_5) andalusite, sillimanite, and kyanite to be stable under geological conditions (Gottschalk 1996; Harlov et al. 2008; Holland and Powell 2011). In natural assemblages, where corundum and quartz occur instead of Al_2SiO_5, the common explanation is that an aqueous fluid catalyzing the reaction must have been missing. For example, granulite facies metapelites of the Bamble

Sector (SE Norway) contain quartz inclusions in corundum, which were interpreted as feature of SiO_2 immiscibility in corundum under dry high $P–T$ conditions (Kihle et al. 2010). According to Kato et al. (2011), a quartz-corundum assemblage within K-feldspar in the Kerala Khondalite Belt (S India) indicates corundum and subsequent quartz growth from a melt at low H_2O activity. Fluid-absent conditions as well as "sluggish diffusion rates of SiO_2 and Al_2O_3" during isobaric cooling are proposed as cause for a metastable reaction of: spinel + quartz → corundum + orthopyroxene, instead of the stable: spinel + quartz → garnet + sillimanite in spinel-bearing quartzites from the Napier Complex, Antarctica (Motoyoshi et al. 1990). Corundum and quartz in nature are thus interpreted to reflect metamorphic or even partly anatectic rocks under "extremely dry conditions" (e.g., Mouri et al. 2003; Kato et al. 2011). This is in stark contrast with the fact that in experiments the metastable assemblage is easily synthesized in the presence of water and the reaction of corundum + quartz to Al_2SiO_5 polymorphs is rarely observed (e.g., Carr and Fyfe 1960; Wahl et al. 1961; Aramaki and Roy 1963).

The transformation reactions between the Al_2SiO_5 polymorphs andalusite, sillimanite, and kyanite are very helpful $P–T$ indicators in Al-rich metamorphic systems, predominantly due to their widespread occurrence in various geological settings and metamorphic facies. However, the synthesis of either of the three polymorphs, e.g., for triple point determination, rarely succeed without the help of natural crystal seeds (Roy 1954; Carr and Fyfe 1960; Althaus 1967; Holdaway 1971; Day 1973; Huang and Wyllie 1974; Kerrick 1990), which suggests that the reaction path $Al_2O_3 + SiO_2 aq → Al_2SiO_5$ is obstructed in some way. Indeed, the only experiments producing Al_2SiO_5 from crystalline Al_2O_3, SiO_2 and water in previous studies have been conducted at pressures ≥ 2 GPa and temperatures ≥ 1000 ℃ (Harlov and Milke 2002).

Why naturally ubiquitous minerals such as the Al_2SiO_5 polymorphs should be so difficult to synthesize is not fully understood. In Schultze et al. (2021) we showed that corundum precipitation next to quartz from various precursor materials and at water saturated conditions involved a nanometer thick hydro-silicate layer inside the corundum crystals as well as on their basal plane, which influenced the crystal growth and shielded the bulk phases from each other, thus likely preventing the reaction towards Al_2SiO_5.

In this study we focus on the formation of silicate mineral reaction rims or coronas on corundum, in order to gain more information on the reaction between corundum and quartz or between corundum and fluid, in which the SiO_2 component is saturated with respect to quartz (called "quartz saturated fluid" hereafter). Corona-formation is particularly well suited as a case study of the interaction of two phases of different composition by the exchange of chemical components. Not only is the reaction site pinned to the interface of the precursor mineral, which precisely locates observations and simplifies interpretations, but the involved reactions are also brought to a halt when a crucial element transport through the corona is inhibited by insurmountably long or obstructed transport pathways (Milke et al. 2001; Harlov and Milke 2002; Lucassen et al. 2010, 2012a, b). Therefore, reactants as well as products preserve information regarding the formation process. Coronas of Al_2SiO_5 polymorphs on corundum may shed light on the interaction of alumina and silica in the system ASH. To our knowledge, attempts of synthesizing aluminium silicate coronas around corundum under realistic metamorphic conditions have never been documented in the literature. In other systems, silicate coronas around oxide single crystals grow readily under metamorphic $P–T$ conditions (> 500 °C; > 0.4 GPa) by exposure of the oxide to quartz saturated fluids. Titanite coronas, for example, were grown on rutile during several hours of interaction with CaO in quartz saturated aqueous solution (Lucassen et al. 2010, 2012a, b).

We conducted experiments exploring the factors controlling or prohibiting the reactions forming aluminium silicates in coronas around corundum using different experimental approaches. Since the system Al_2O_3-SiO_2 is known for its sluggish reaction kinetics (Tracy and McLellan 1985), all experiments were carried out in the presence of excess aqueous fluid, some with additional acidic solutes, to ensure sufficient element mobility (Salvi et al. 1998). In doing so, a steep chemical potential gradient was created at the surface of corundum single grains that was used to test and exclude potentially reaction-inhibiting factors during the interaction of corundum and aqueous silica towards kyanite or sillimanite at $P–T$ conditions close to natural examples (< 1000 °C; < 2 GPa). The corundum's response to the attacking silica-rich agent was documented on the nanometer scale, providing detailed insight into the interactions of all involved components.

Experiments

Corundum single crystals were exposed to quartz saturated aqueous fluids or silica releasing dehydrating mineral matrices in 29 experimental runs using five different setups under conditions within the stability field of kyanite or sillimanite. The principle setups are described below and the compositions, P–T conditions, and run times are listed in Table 1. Some experiments were seeded with crushed natural kyanite, and for comparison, experiments with additional solutes (K^+, Na^+, Mg^{2+}, NH_4^+) besides silica and one experiment with baddeleyite instead of corundum was also performed. The different setups were chosen to differentiate between

Table 1 Experiments on corundum single crystal interaction with silica and water saturated environment: experiments with P–T > 700; > 0.52 GPa were conducted in a piston cylinder press

Run number	Setup	Crn/Bdy [mg]	SiO$_2$ [mg]	H$_2$O [mg]	Additional solute [mg]		P [Gpa]	T [°C]	t [d]	Als stability field
1	1	14.21	12.04	16.34	–		0.5	500	26	Ky
2	1	7.67	8.44	22.81	BH$_3$O$_3$	5.54	0.5	500	26	Ky
3	1 (ic)	1.95	3.85	7.98	HCl	2.66	0.47	500	14	Ky
4	1 (ic)	2.84	1.56	9.95	HCl	3.32	0.47	500	33	Ky
5	1 (ic)	1.84	0.47	2.56	HCl	0.85	0.47	500	7	Ky
6	1 (ic)	8.83	1.20	1.62	HCl	0.54	0.48	500	23	Ky
7	1 (ic)	10.45	2.07	1.92	HCl	0.64	0.48	600	23	Sil
8	1 (ic)	8.61	1.76	47.54	HCl	15.85	0.5	500	31	Ky
9	1 (ic)	9.34	2.34	10.31	HCl	3.44	0.5	500	13	Ky
10	1	8.05	10.55	13.28	HCl	4.43	0.5	500	24	Ky
11	1	14.18	3.54	8.14	HCl	2.71	0.5	500	14	Ky
12	2	5.34	20.51	6.46	–		1	800	5	Ky
13	2	6.91	1.92	9.05	HCl	3.02	0.47	500	33	Ky
14	2	2.21	1.62	2.27	HCl	0.76	0.47	500	7	Ky
15	2	8.19	2.70	10.12	HCl	3.37	0.5	500	13	Ky
16	3 (ic)	3.54	2.13	10.12	NaCl	0.26	0.52	500	6	Ky
17	3 (ic)	4.93	1.97	11.30	NaCl	0.29	0.52	500	6	Ky
18	3 (ic)	1.87	2.65	11.29	NaCl	4.03	0.38	700	21	Sil
19	3 (ic)	6.03	4.87	4.20	NaCl	0.12	0.5	500	31	Ky
20	3 (ic)	1.29	3.01	11.20	KCl	0.01	0.47	500	14	Ky
21	3 (ic)	1.84	2.87	11.19	KCl	0.07	0.47	500	14	Ky
22	3 (ic)	2.26	2.10	12.33	KCl	0.76	0.49	500	21	Ky
23	3 (ic)	12.00	2.74	11.35	KCl	0.70	0.38	700	21	Sil
24	3 (ic)	13.86	4.64	11.00	NaOH	0.44	0.49	500	21	Ky
25	3	8.27	3.23	12.71	NaOH	0.50	0.49	500	21	Ky
26	3	6.71	25.9	11.20	NH$_3$OH	3.73	0.5	650	21	Sil
27	3	8.46	2.99	12.15	MgO	3.28	0.2	650	12	Sil
28	4	3.00	12.84	12.20	–		0.5	650	21	Sil
29	5	21.56	16.17	–	Ms	71.54	0.48	690	13	Sil

Als aluminium silicate, "(ic)" refers to the use of a perforated internal capsule

influences of properties of the solid reactants, the fluid, and the precipitating phases on the occurring reactions.

Setup 1: corundum + SiO$_2$aq + H$_2$O ± HCl ± BH$_3$O$_3$

The experiments of this series were designed to investigate the interaction of the corundum single crystals with pure, quartz saturated aqueous fluid, which should theoretically proceed according to reaction R1:

$$Al_2O_3 + SiO_2aq \rightarrow Al_2SiO_5 \qquad (R1)$$
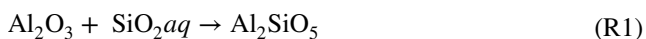
Amorphous SiO$_2$ was used as silica source. Additional experiments with variable pH were conducted (Carroll-Webb and Walther 1988; Pokrovski et al. 1996; Salvi et al. 1998) because the solubility of Al in aqueous fluid of near neutral pH is known to be extremely low (Anderson and Burnham 1967; Burnham et al. 1973; Becker et al. 1983; Ragnarsdottir and Walther 1985; Walther 1997; Mookherjee et al. 2014), which could affect the tendency of the system to nucleate Al$_2$SiO$_5$ polymorphs. pH neutral experiments contained deionized water, whereas in variably acidic (down to pH = 0) experiments either BH$_3$O$_3$ or HCl was added to the assemblage (Table 1). Experimental *P–T* conditions were set to 500–600 °C; 0.47–0.5 GPa. To prevent direct contact of corundum crystals and the silica reactant and to assure interaction of the corundum with the silica bearing fluid only, the corundum grains in some experiments were enclosed in perforated inner gold or platinum capsules (1 mm outer diameter, 5 mm length, indicated with "ic" in Table 1).

Setup 2: corundum + SiO₂aq + H₂O + kyanite ± HCl

To investigate a potential nucleation inhibition of aluminium silicates, experiments were performed under similar conditions as in setup 1 at 500–800 ℃; 0.47–1 GPa (Table 1) but with the addition of kyanite seed crystals in contact with the corundum grains. This was meant to show whether a kyanite corona would start to grow from kyanite seeds in case the nucleation rate of kyanite was too low for the reaction to occur spontaneously.
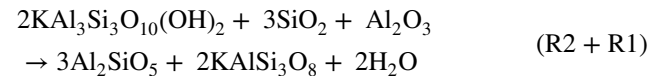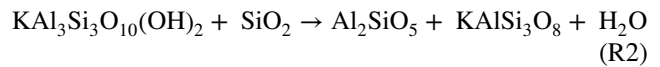
Setup 3: corundum + SiO₂aq + H₂O + additional cations

Experiments were conducted with corundum single crystals and different additional cations (K^+, Na^+, Mg^{2+}, NH_4^+) in solution, in addition to SiO_2. Varying concentrations of NaCl, KCl, NaOH, NH_3OH, or MgO were added to the deionized water (Table 1). Anticipated reaction products were muscovite (Ms, $KAl_3Si_3O_{10}(OH)_2$), orthoclase (Or, $KAlSi_3O_8$), paragonite (Prg, $NaAl_3Si_3O_{10}(OH)_2$), albite (Ab, $NaAlSi_3O_8$), clinochlore (Clc, $Mg_3Al_2Si_3O_{10}(OH)_8$), and buddingtonite (Bud, $(NH_4)AlSi_3O_8$). Experimental conditions were set in a range of 500–700 ℃ and 0.2–0.52 GPa (mineral abbreviations according to Whitney and Evans 2010).

Setup 4: baddeleyite + SiO₂aq + H₂O

To monitor whether the quartz saturated aqueous fluid, which is a very rough approximation of a natural metamorphic fluid (e.g., Yardley and Cleverley 2015) , unfavorably influences the precipitation of silicates on oxide crystals in general, baddeleyite (Bdy, ZrO_2) crystals were used instead of corundum with the aim of producing a zircon (Zrn, $ZrSiO_4$) corona. The systems Al_2O_3-SiO_2 and ZrO-SiO_2 have significant similarities making them ideal for comparison. Baddeleyite has a very low solubility in most aqueous fluids similar to corundum (Migdisov et al. 2011). The Al_2SiO_5 polymorphs and zircon are all orthosilicates (or nesosilicates), thus when precipitating from a fluid the silica component is required not to polymerize. The structural differences between oxides and silicates of both systems do not allow topotactic replacement, as for example during albitization of feldspars (or dissolution-reprecipitation reactions, see Putnis (2002); Putnis and Austrheim (2010). Instead a dissolution–precipitation mechanisms (Lucassen et al. 2010) is required. The assemblage baddeleyite and deionized water plus silica was heated to 650 °C, at 0.5 GPa (Table 1).

Setup 5: corundum + muscovite + quartz

In order to simulate approximate natural observations of sillimanite growth during muscovite breakdown according to reaction R2, corundum single crystals were embedded in a matrix of natural muscovite and quartz (molar ratio Ms:Qz = 2:3), without added fluid, and heated to 690 °C; 0.48 GPa.

$$KAl_3Si_3O_{10}(OH)_2 + SiO_2 \rightarrow Al_2SiO_5 + KAlSi_3O_8 + H_2O \quad (R2)$$

$$2KAl_3Si_3O_{10}(OH)_2 + 3SiO_2 + Al_2O_3 \\ \rightarrow 3Al_2SiO_5 + 2KAlSi_3O_8 + 2H_2O \quad (R2 + R1)$$

Starting materials

Natural and synthetic minerals as well as analytic-grade chemicals were used (Table 1). Chemical analyses and specific details for those starting materials are given in Electronic Supplementary Material as (e.g., Online Resource 1). Both natural and synthetic corundum single crystals were used simultaneously in most experiments to check if the nature of the corundum has an influence on the results.

Experimental apparatus

Hydrothermal experiments up to 0.52 GPa and 700 ℃ were conducted in externally heated cold-seal vessels in a hydrothermal apparatus using water as pressure medium at Technische Universität Berlin. For pressures of 1 GPa, a piston cylinder experiment was conducted in a non-end loaded piston cylinder press ("Johannes"-type) at Geo-ForschungsZentrum Potsdam. Details about the experimental assemblies are given in the Electronic Supplementary Material and in Schilling and Wunder (2004).

Preparation, analytical methods

At the end of each experimental run, the cold seal vessels were quenched in an air stream to < 100 °C within approximately 5 min. The removed capsules were weighed to detect potential fluid loss during the experiment. Capsules were opened, pH values of the extracted fluids were determined and the solid run products were dried. Single crystals were mounted along with the fine-grained powder products on specimen holders for scanning electron microscopy (SEM) analysis first and in a second step the products were embedded in epoxy and prepared for electron microprobe (EMP) analysis. The entire capsule from setup 5 and from the piston cylinder experiment run 12

(setup 2) was cast in epoxy, cut into slices, and mounted directly on glass slides in order to preserve experimental textures.

SEM analyses were conducted at Technische Universität Berlin using a Hitachi S-520 SEM. Field emission microprobe (EMP) analyses were conducted with a JEOL JXA-8530F at Technische Universität Berlin. After thorough microprobe investigations, approximately $15 \times 7 \times 0.15$ μm large foils were cut from selected areas in thin sections by focused ion beam (FIB) milling method under ultra-high vacuum conditions using a FEI FIB200 instrument at GeoForschungsZentrum Potsdam. The foils were then placed on a perforated carbon film and analyzed with an FEI Tecnai G2 F20 X-Twin transmission electron microscope (TEM) with a field emission gun as electron source. Details about analytical conditions as well as reference materials used are given in the Electronic Supplementary Material.

Results

No Al_2SiO_5 polymorphs formed in unseeded experiments nor did the kyanite seeds grow in the seeded experiments. Instead, various other features of interaction between Al_2O_3 and SiO_2 were observed in different stages of the experiments, as well as the growth of the metastable assemblage of corundum plus quartz. The different observations will be presented sorted by experimental setup.

Setup 1: corundum + $SiO_2 aq$ + H_2O ± HCl ± BH_3O_3

The interaction of corundum with neutral, quartz saturated water (run 1; Table 1) resulted in a complete, yet porous quartz cover on the corundum grains (Online Resource 2). With decreasing pH the quartz cover on corundum became increasingly incomplete and intense etch pit formation was observed on the corundum surface (Fig. 1). In experiments with neutral or moderately acidic pH (run 1, and 2) the dissolution features at the corundum surface appeared to be prominently influenced by fluid pathways (preserved as fluid inclusion trails) through the growing quartz crystal cover (Fig. 1a, b, Online Resource 2). Topographic depressions in the corundum were either found at the contact of the corundum surface with quartz-quartz grain boundaries (Fig. 1b, Online Resource 2) or, in the case of incomplete quartz covers, where there was no quartz on the corundum surface (Fig. 1a), while the dissolution of corundum at positions covered by quartz appeared limited and formed hill-like features (Fig. 1a). Moreover, the covered parts of corundum were occasionally enclosed and isolated by quartz and eventually detached from the large single crystal (Fig. 1a, b).
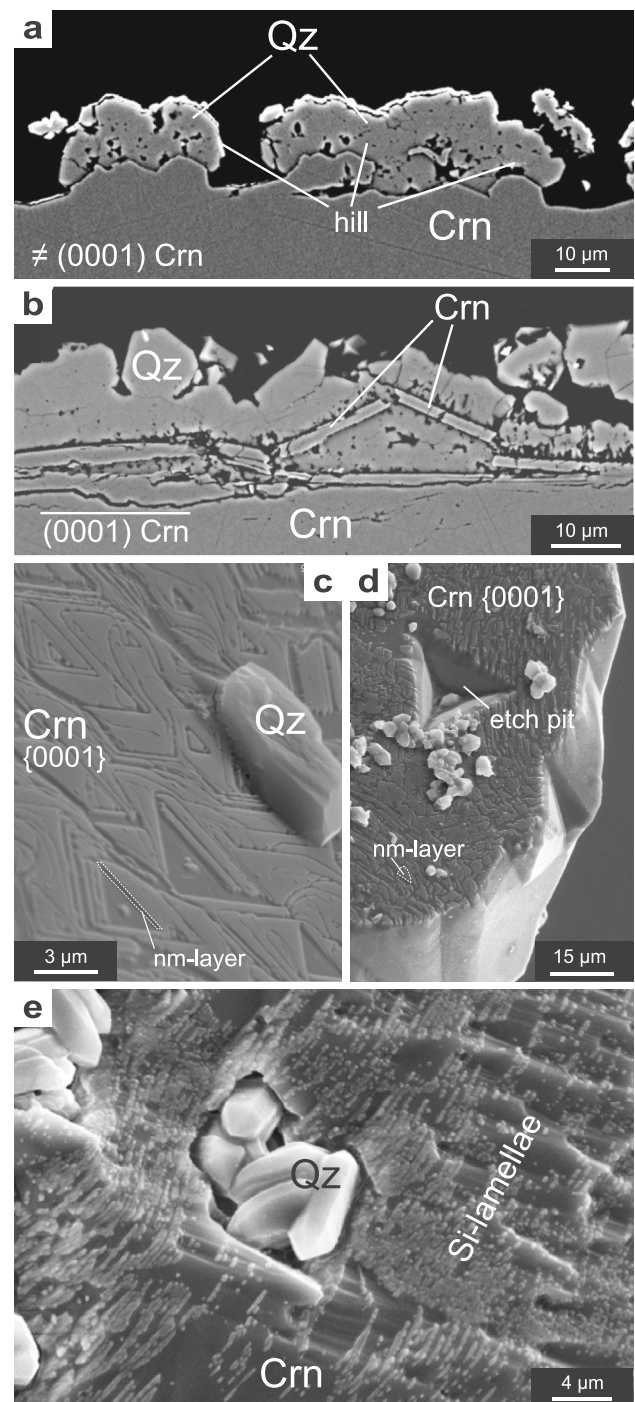
Fig. 1 Altered corundum from Setup 1 and 2, with low pH: **a** and **b** are H_3BO_3 added run 2. **c**, **d**, and **e** are HCl added runs 4, 13, and 3. **a** and **b** BSE images (EMP) of dissolution features along the corundum (Crn) surface. **a** Crn face oblique to {0001} shows a valley-and-hill-morphology evolved beneath an incomplete quartz (Qz) cover, with detached Crn inclusions in Qz grains. **b** Qz cover grown on {0001} face of Crn without valley and hill morphology, instead plates of Crn are detached parallel to {0001}. **c** SE image of shallow etch pits formation on {0001} faces indicates limited Crn dissolution in [0001]. **d** Only one prominent etch pit with dissolution planes in {10-12} is found on {0001} (SE image). In both **c** and **d** a silica bearing, ca. 200 nm wide layer is displayed on the Crn basal plane (Online Resource 3 and 4). Shallow etch pits are carved into this layer. **e** SE images of etched Crn surface, covered in < 1 μm thick, strictly parallel oriented, Si-bearing lamellae (brighter than Crn surface). Qz is grown into the Crn surface

Dissolution features recovered from synthetic corundum grains revealed that they varied on different faces (Fig. 1a, b). The polished basal plane rarely showed etch pit formation. Instead, plates of corundum were detached parallel to {0001} and enclosed by quartz (Fig. 1b). Only long experimental runs of more than 14 days with HCl (runs 4, 6, 7, 8, 10) showed characteristic trigonal, generally shallow (< 1 μm deep) etch pits on the {0001} faces (Fig. 1c, d). These etch pits are depressions in an up to 500 nm wide, Si-rich (0001) corundum surface layer on strongly etched synthetic corundum grains (Fig. 1c, d, Online Resource 3, Online Resource 4). SiO_2 and Al_2O_3 concentrations obtained by EMP analyses along the layers are highly variable due to edge effects caused by uneven phase boundaries (Online Resource 4). {10–12} and occasionally {− 1014} formed prominent etch pit faces during those runs (Fig. 1d, Online Resource 3).

While dissolution features were common on the corundum surfaces, no evidence for precipitation of corundum was found in any of the experiments using setup 1. Independent of the intensity of corundum dissolution (inferred from etch features), no precipitation of any of the Al_2SiO_5 polymorphs was observed. Instead, Al-Cl bearing quench products associated with quartz grains were found in runs containing HCl. Synthesized quartz grains showed elevated Al concentrations of up to 0.5 wt% Al_2O_3 in both neutral and acidic experiments.

Experiments with a duration of ≤ 14 days produced etched corundum grains (synthetic and natural) interspersed with single quartz grains grown several μm into the corundum surface (Fig. 1e). The corundum surface was covered with up to 1 μm thick, parallel oriented, Si-bearing lamellar and planar features (Fig. 1e). Cross sections through natural corundum single grains showed an up to 50 μm wide, altered area in the margin of the grains (visible in both CL and BSE images), where the Si content of the corundum increases substantially to up to 5000 ppm (Fig. 2a, b, c). The Si distribution in the rim appears to be heterogeneous, with maximum Si concentrations along parallel, up to 1 μm thick layers or stripes within the grain (Fig. 2c), which likely correspond to the lamellar and planar Si-rich features observed at the corundum surface (Fig. 1e). An element-profile was measured perpendicular to the stripe pattern of Si in the reaction rim. The highest Si contents were measured along the reaction front (Fig. 2c, profile *A-B* see Table 2). Silicon concentrations decrease continuously in the altered rim and towards the corundum surface, but still exceed the Si concentration in the non-altered grain (Fig. 2c, Table 2). The Si profile resembles a steep ramp (Fig. 2c). Iron contents of 0.04–0.08 wt% Fe_2O_3 in unaltered natural corundum are depleted in the reaction rims to < 0.03 wt% or values below detection limit (Table 2, Fig. 2c).

Reaction rims on natural corundum crystals were significantly wider than those on synthetic grains. The latter were generally not more than 1 μm wide and covered grains less comprehensively than the rims on natural grains, making it difficult to investigate the rims on synthetic grains.

Transmission electron microscopy (TEM) investigations carried out along the element profile in Fig. 2c showed that the Si increase in the altered corundum rim is related to hydro-silicate nano-layers (hereinafter called HSNL) oriented along and replacing the Al-octahedral basal plane of the corundum and replacing the Al-octahedral layers (Fig. 3). The first 200 nm of the reaction front (measured from the inside out) are enriched in Si but no specific features in the corundum related to the enrichment were identified in bright field images or high-resolution TEM (HRTEM; Fig. 3a). Behind the 200 nm front, homogeneously distributed and strictly oriented individual HSNL were found (Fig. 3a). Throughout the rest of the alteration rim starting 200 nm away from the reaction front and ending at the corundum surface, however, the HSNL appeared increasingly organized or accumulated in restricted, parallel oriented areas separated by HSNL-free corundum (Fig. 3b).

An energy dispersive X-Ray spectroscopy (EDS) profile through the HSNL and HSNL-free corundum is shown in Fig. 3c. The calculated quantitative results lie within the range of uncertainty of the analytical method of ≤ 5% for elements with an atomic mass number > 8 (oxygen). An inverse trend is observed between the Si- and Al-profile with on average ca. 4 atomic % less Al in the HSNL compared with the layer free corundum and ca. 2% more Si (Fig. 3c). In bright field (BF) images and in Si element mappings alike, the accumulated layers are visible as a stripe pattern (Fig. 2c, Fig. 3b). Analytical electron microscopy (AEM) and electron energy loss (EEL) analyses were conducted on homogeneously distributed individual HSNL within the reaction front (II in Fig. 3a) and in densely stacked areas (III in Fig. 3b) as well as on nanolayer free corundum (I in Fig. 3b). Analyses in II and III showed that Al is substituted by Si and OH (Fig. 3d). HRTEM images taken with the incident beam parallel to $(0001)_{Crn}$ within the reaction rim showed the same atomic features and substitution of Al-octahedral layers by Si and OH that was observed inside and on the $[0001]_{Crn}$ surface of corundum precipitates in Schultze et al. (2021) (Fig. 4). Diffraction patterns of altered corundum, which shows HSNL in high angular annular dark field (HAADF) images display a weak additional diffraction peak halfway between (0000) and (0006), indicating double lattice plane distance (Online Resource 5). Electron diffraction patterns display the HSNL as streak pattern in [0001] (Online Resource 5) thus indicating the presence of very thin (few nm) platelets normal to the streaking.

Despite the intense interaction of corundum and silica within the altered rims, aluminium silicate precipitation was

Fig. 2 **a** Optical cathodoluminescence (CL) image of an altered natural corundum (Crn) grain from run 3 with a marginal, up to 50 μm wide, reaction rim (reaction front indicated with white dashed line). **b** Detail BSE image of the reaction rim (brighter than the unaltered Crn) containing two quartz (Qz) inclusions. **c** Element mapping of Si (produced at 20 kV, 100 nA, 500 ms dwell time) of the area in **b** combined with an element profile *A-B* (Table 2). The map displays Si increase and heterogeneous Si distribution (stripe pattern highlighted with fine, white, dashed lines) in the rim compared with the unaltered Crn grain. Al and Si trends in the element profile are inverse, Si-maxima are measured in the reaction front, and the rim is depleted in Fe (Al_2O_3 in wt%, Si, and Fe in ppm, absolute counting statistical uncertanties are indicated as shaded range and given in Table 2)
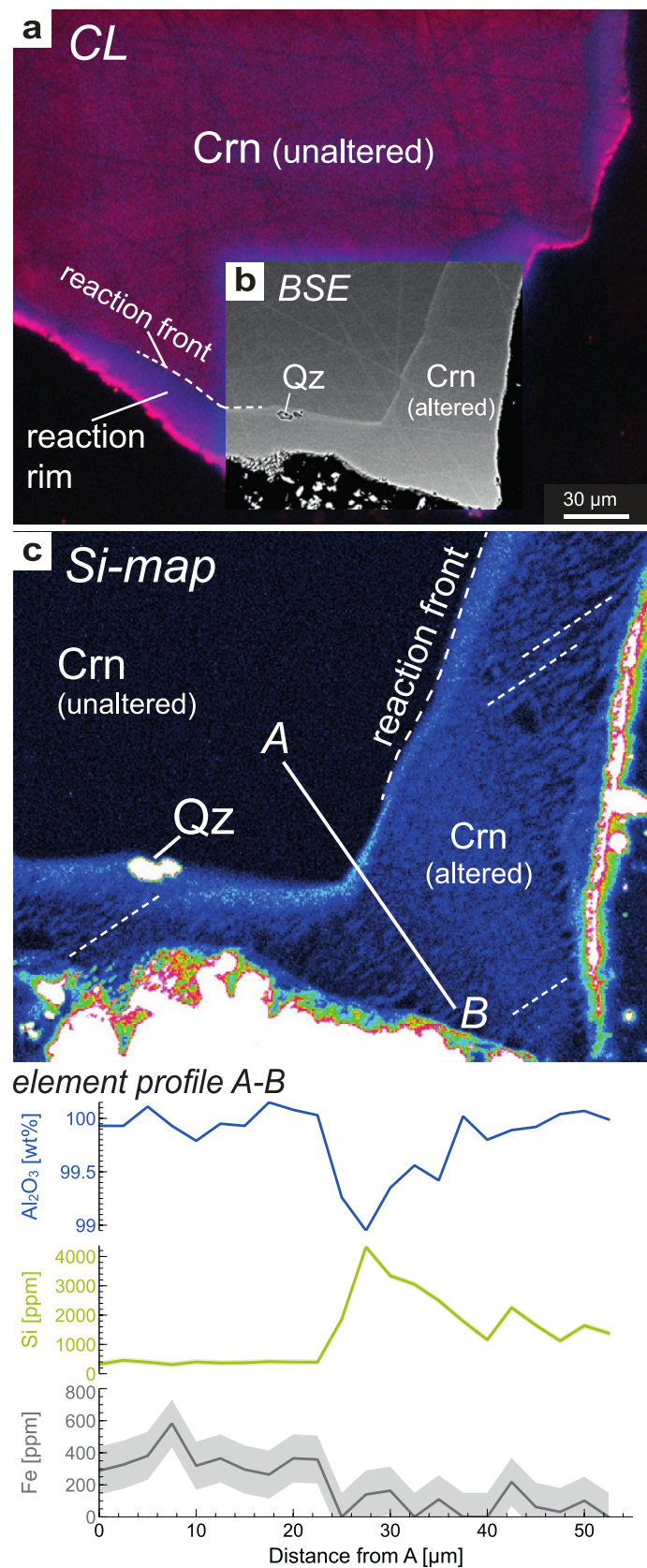
Table 2 Compositional profile A-B (in oxide wt%, 1 analysis point per 2.5 µm) through Si-enriched reaction rim in corundum single grain in run 3: 500 ℃; 0.47 GPa, see Fig. 2c (WDS results EMP)

µm	0	2.5	5	7.5	10	12.5	15	17.5	20	22.5	25	27.5
SiO_2	0.07	0.10	0.08	0.07	0.09	0.08	0.08	0.09	0.09	0.08	0.40	0.93
Al_2O_3	99.93	99.93	100.11	99.93	99.79	99.95	99.93	100.15	100.08	100.03	99.26	98.95
Fe_2O_3	0.04	0.05	0.05	0.08	0.05	0.05	0.04	0.04	0.05	0.05	0.00	0.02
Total	100.04	100.07	100.25	100.08	99.92	100.08	100.05	100.28	100.22	100.17	99.66	99.90
Si ppm	323	458	393	309	402	365	374	411	397	393	1856	4324
Fe ppm	288	326	381	583	319	365	295	264	365	358	0	140
µm	30	32.5	35	37.5	40	42.5	45	47.5	50	52.5	D.L.	c.s.u
SiO_2	0.72	0.65	0.53	0.38	0.25	0.48	0.35	0.24	0.35	0.30	0.02	0.01
Al_2O_3	99.35	99.56	99.42	100.02	99.80	99.89	99.92	100.04	100.07	99.99	0.02	0.11
Fe_2O_3	0.02	b.d	0.02	b.d	b.d	0.031	0.01	b.d	0.02	b.d	0.01	0.02
Total	100.09	100.21	99.97	100.40	100.05	100.40	100.28	100.28	100.44	100.29	–	–
Si ppm	3342	3048	2496	1795	1159	2253	1655	1122	1641	1384	–	–
Fe ppm	163	0	109	0	0	218	62	31	101	0	–	–

Unreacted corundum areas in *italic*, Limits of detection "D.L." and absolute counting statistical uncertainty (1 σ) "c.s.u." are indicated

not observed. Instead, up to 10 µm large quartz inclusions were occasionally found inside the altered corundum rim, distant from the single crystals surface (Fig. 2b, c). Furthermore, the HSNL-bearing altered corundum areas disappeared in experiments after 21 days. No clear evidence was preserved at the corundum surface that could indicate what happened to the altered rim areas. However, altered areas were also found around fluid inclusion trails inside the corundum grain after ≤ 14 days (Fig. 5a, profile *AA-AB* see Online Resource 6). Similar inclusion trails hosted numerous quartz grains and fluid after longer experiments, while no increase in Si or other signs of alteration could be detected in corundum areas enclosing the trail (Fig. 5b, c).

Setup 2: corundum + SiO₂aq + H₂O + kyanite ± HCl

Kyanite-seeded experiments with hydrochloric acid (runs 13–15, Table 1) showed dissolution features predominantly along the kyanite cleavage. The features became more pronounced with increasing run time. Piston cylinder experiment (run 12) with pure water resulted in corundum grains rich in fluid inclusion trails, pressure twins, and signs of corundum dissolution. Kyanite seeds placed on the corundum, however, showed no sign of growth (Online Resource 7a, b). Despite clear signs of deformation, e.g. kink features, resulting from the compressional stress during the experiment, no evidence of growth, (re-)crystallization or dissolution of the kyanite could be observed. EMP element maps clearly show increased Si concentrations around fluid inclusion trails in corundum, indicating that the lack of kyanite growth was not caused by lack of interaction of silica-bearing fluid with kyanite and corundum. Furthermore, the perforated Pt-capsule used in run 12 partly dissolved

and left clear evidence of fluid transport through the kyanite grain boundaries and into the corundum by re-precipitating Pt (Online Resource 7b).

Setup 3: corundum + SiO₂aq + H₂O + additional cations

The interaction of corundum single crystals and fluids containing additional cations K⁺, Na⁺, Ca²⁺, Mg²⁺, and NH₄⁺ besides silica resulted in moderate dissolution features on the corundum surface at lower concentrations of the solutes (e.g., KCl < 0.08 molal; run 20). The addition of NaCl did not result in the formation of solids independent of NaCl concentration, instead the experiments contained Si and Na-bearing quench products with highly variable amounts of Al and Cl. At higher concentrations of KCl, NaOH, NH₃OH, and MgO (runs 21–27) and depending on the temperature of the experiments, phyllosilicates muscovite (Ms), paragonite (Prg), and clinochlore (Clc) (Online Resource 8a, b) and/or feldspars orthoclase (Or), albite (Ab), and buddingtonite (Budd) (Online Resource 8c) formed. MgO-bearing experiments produced complete clinochlore coronas on corundum, in addition to which forsterite also formed (Online Resource 8a, b).

The appearance of the corona was mostly defined by the newly formed products. While phyllosilicate coronas (Ms, Clc) were fine grained, porous and occasionally formed pseudomorphic replacement features on corundum (Online Resource 8a, b), buddingtonite formed fewer but larger, euhedral grains that enclosed corundum and quartz remnants without a visible crystallographic relationship between the reactants and the product (Online Resource 8c). A common observation in all experiments (except the one with NH₃OH, due to intense Crn dissolution) was
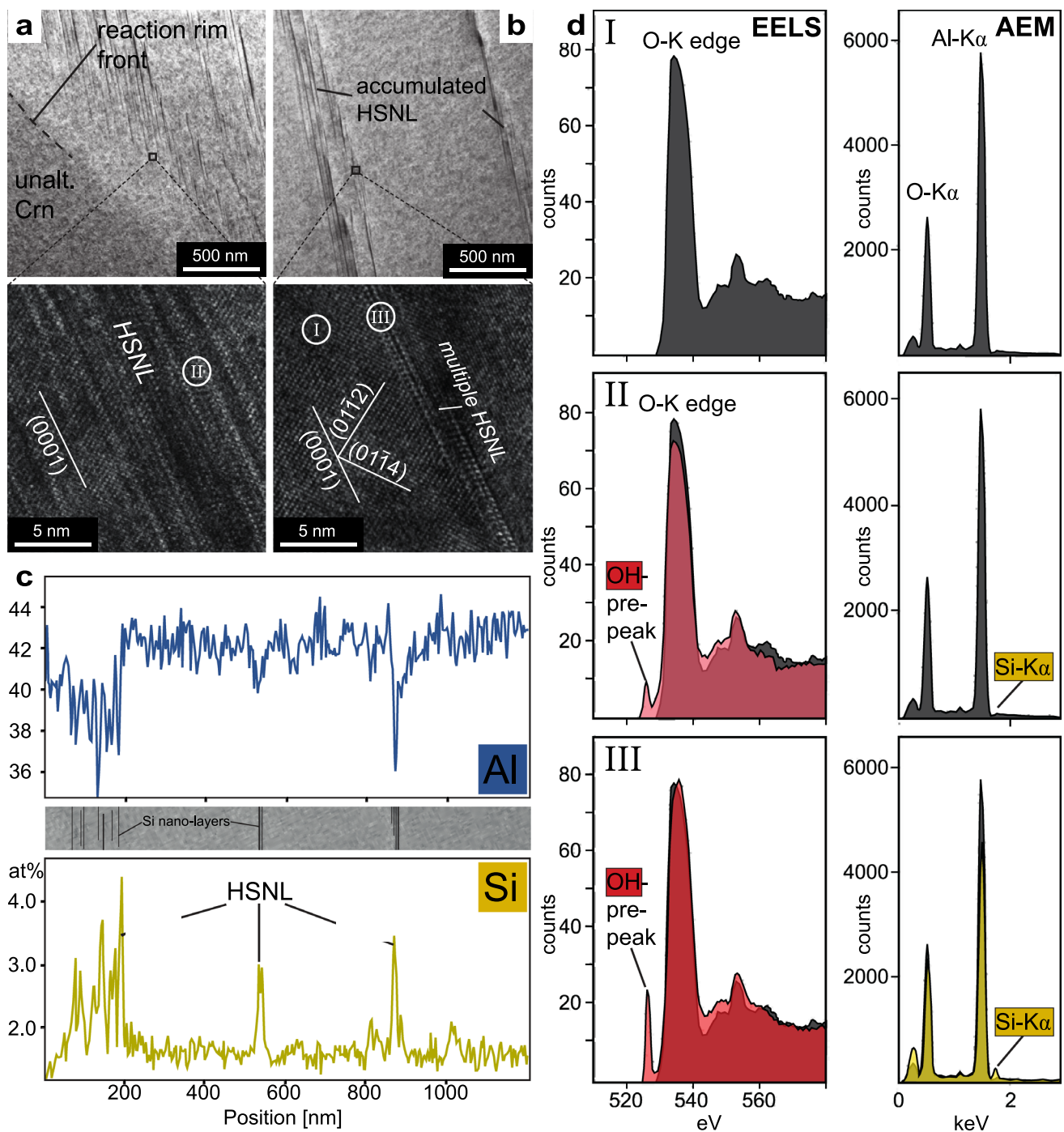
Fig. 3 Transmission electron microscopy (TEM) investigations on the altered corundum rim from Figure 2 (run 3). **a** Bright field (BF) image of the reaction rims front (dashed line) and unaltered Crn (left) with corresponding HRTEM image inside the reaction front (lower image). Hydro-silicate nano-layers (HSNL) are homogeneously distributed within the first 200 nm of the front and strictly parallel oriented to {0001} in Crn. **b** BF image of the reaction rim within 5 μm distance to the reaction front **a** with corresponding HRTEM image (lower image).With increasing distance to the diffusion front the HSNL generally appear in pairs or groups accumulated in restricted areas (up to 0.5 μm) in otherwise unaltered Crn. **c** EDS element profile of Si (yellow) and Al (blue) (in atomic %) measured through areas of areas with high HSNL density and areas of unaltered Crn (see modified BF image stripe between the profiles). Al and Si are negatively correlated (error ca. 5%). d TEM-electron energy loss spectroscopy (EELS, left side) and analytical electron microscopy (AEM, right side) analyses of unaltered Crn (I), Crn within the reaction front including individually distributed HSNL (II), and Crn including multiple accumulated HSNL (III) [I-III are indicated in **a** and **b**]. (I) is free of OH bonds and Si since no OH-pre-peak at 528 eV in the EELS spectra (see Wirth and Wunder 2000) and no Si–Kα peak (AEM) are visible, (II) and (II) show increasingly high OH-pre-peak and Si–Kα peak correlating with increasing HSNL density
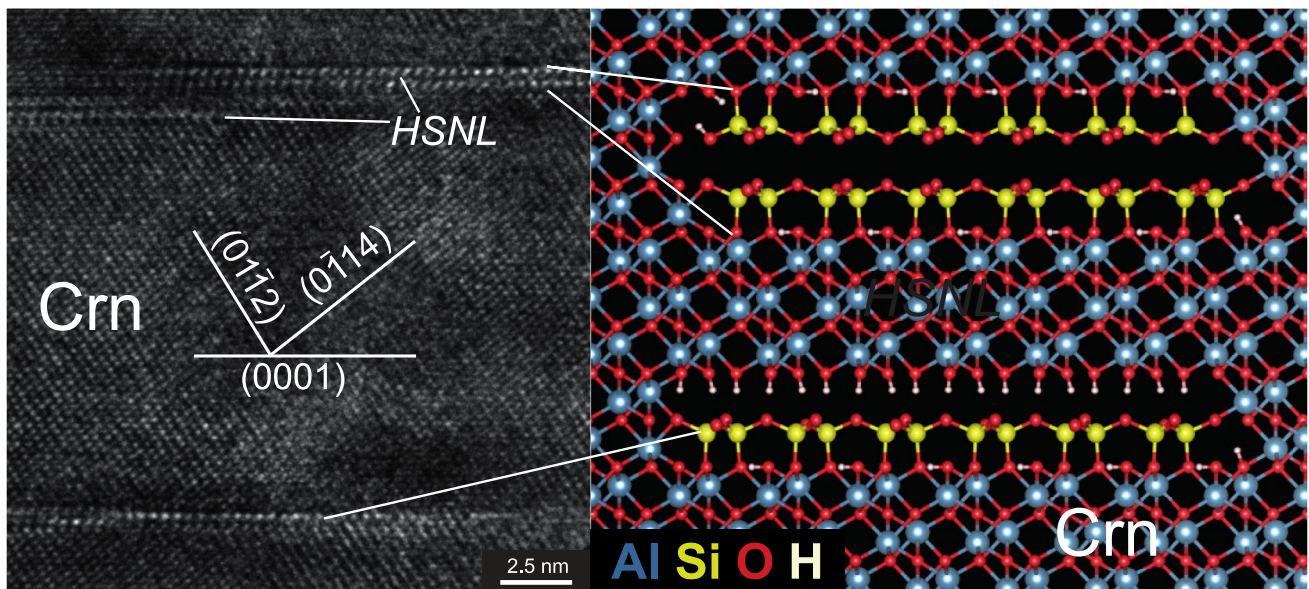
Fig. 4 On the left; HRTEM image inside the corunudm reaction or Si diffusion rim around 1 μm away from the reaction front (run 3, Setup 1). On the right; atomic model of the HSNL: $Si4+_{4+}$ in yellow, Al_{3+} in blue, O_2- in red, H_+ in white: the layers are strictly parallel oriented to {0001} in Crn and they appear as silica tetrahedral double (top) or single layers (bottom) replacing three or two Al-octahedral layers respectively (the reaction is charged balanced with H_+) (crystal structure models were made with VESTA "Visualization for Electronic and STructural Analysis" by Momma and Izumi 2011). The molecular structure resembles incomplete structures of pyrophyllite and kaolinite
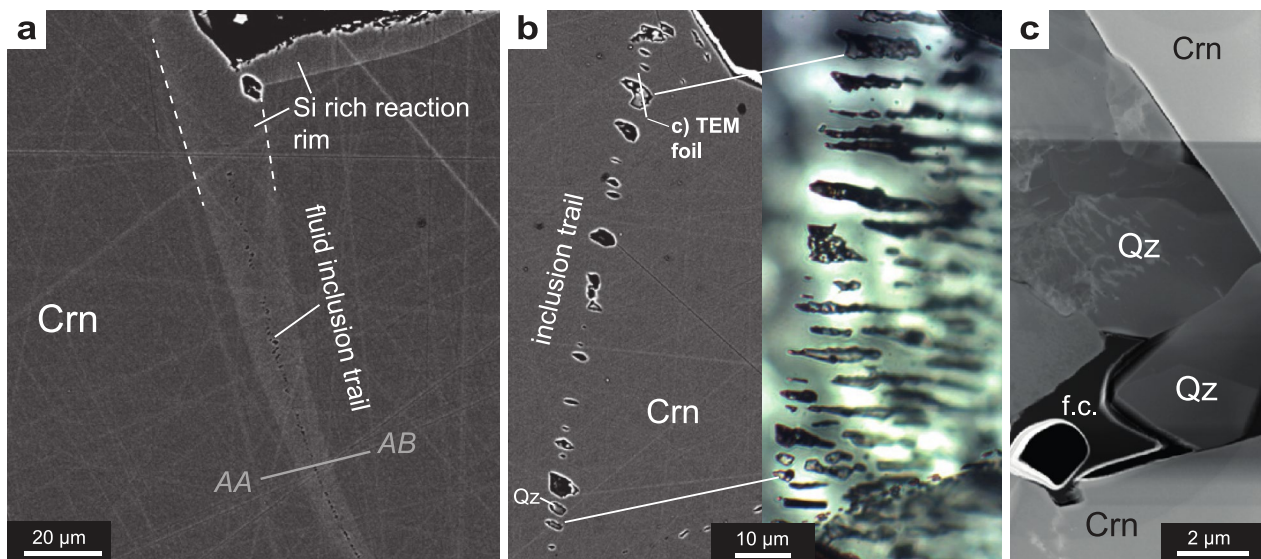
Fig. 5 Natural corundum single crystals after **a** 14 days (run 3) and **b** and **c** 33 days of runtime (run 4, Setup 1, HCl added). **a** After 14 days of experiment Si rich reaction rims are found along fluid trails in Crn (BSE image). A chemical profile *AA-AB* through the altered area around the fluid trail is indicated and data is given in Online Resource 6. **b** After 33 days of experiment, quartz grains are found along former fluid inclusion trails (left: BSE image and right: microphotograph of the Qz hosting trail). The Crn adjacent to the inclusions appears unaltered (no Si-rich reaction rim). **c** HAADF image of a TEM foil cutting through Qz hosting inclusion (indicated in **b**). Several Qz individuals are associated with a fluid cavity (f.c.)
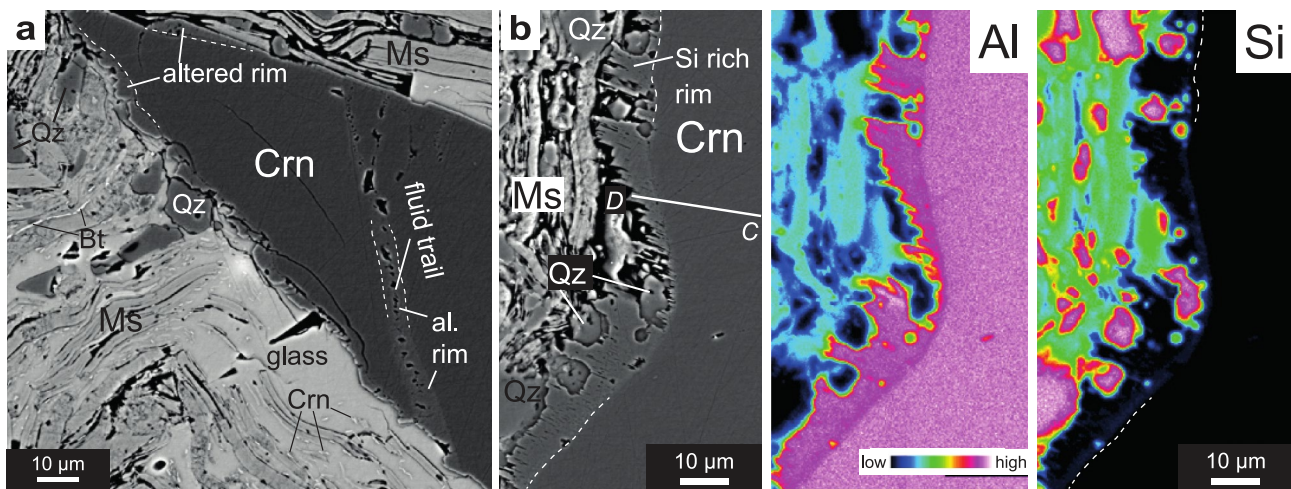
Fig. 6 Experimental product of Setup 5 (run 29): natural corundum (Crn) grain in muscovite-quartz matrix. **a** After two weeks of experiment the muscovite (Ms) is partly decomposed forming a heterogeneous glass with local orthoclase (Table 3) that is mainly located around the Crn single crystals and contains rounded Qz grains and tiny Crn plates (bright in BSE). Si rich reaction rims are developed at the Crn surface and along fluid trails. **b** Left: BSE images of a Si rich reaction rim in Crn at the Crn-matrix interface (chemical profile C-D through rim and unaltered corundum is indicated, data is given in Table 4), with corresponding Al and Si element mappings on the right (conducted at 20 kV, 50 nA, 100 ms dwell time). The outermost part of the rim consists of plate like Crn, that might be the result of epitactic growth of Crn precipitates from muscovite breakdown onto the Crn single crystal surface. The reaction rim locally contains up to 4 wt% SiO_2 whereas Al contents are slightly decreased (see Al and Si mappings, and Table 4)

Table 3 Run 29 (setup 5) glass and/or orthoclase composition (oxide wt%) formed after muscovite dehydration (WDS results, EMP), ordered by SiO_2 content

	Glass Near Crn	Glass/or? Distant fr. Crn	Or	Or	Or	Glass	Glass	Glass	Glass Near Qz
SiO_2	79.86	67.10	65.25	64.26	63.94	61.57	61.65	55.77	51.19
Al_2O_3	8.71	18.97	18.52	19.74	19.50	17.44	18.84	26.04	27.11
Na_2O	0.00	1.32	1.44	1.60	1.52	1.31	1.66	1.46	0.97
K_2O	0.00	13.44	14.99	14.77	14.98	13.71	14.65	13.44	9.70
FeO	b.d	b.d	b.d	0.04	0.06	b.d	b.d	0.10	b.d
Total	88.57	100.82	100.19	100.44	100.06	94.03	96.86	96.87	88.98
A/NK	–	1.13	1.00	1.06	1.04	1.03	1.01	1.54	2.24

$A/NK = Al_2O_3/Na_2O + K_2O$ (molar)

that the polished basal plane of synthetic corundum single crystals barely displayed etch pits or at least distinctively less pronounced than other areas of the crystal. Also, the basal plane was generally corona-free, even if the rest of a grain was entirely corona-covered.

Setup 4: baddeleyite + SiO_2aq + H_2O

An up to 5 μm wide, continuous zircon corona had formed on baddeleyite in quartz saturated deionized water after 21 days (Online Resource 9a, b). Porous assemblages of anhedral to subhedral zircon crystals (up to 5 μm in size) and scattered quartz grains (< 2 μm) were found along open cleavage planes or cracks inside baddeleyite (Online Resource 9a, b). The zircon corona was covered by an up to 20 μm thick quartz coat, the quartz grains of which were occasionally grown directly on the baddeleyite surface (Online Resource 9b).

Setup 5: corundum + muscovite + quartz

Between only partly decomposed muscovite and strongly etched quartz grains, the products of this experiment (run 29, Table 1, run time of 2 weeks) were mainly composed of interstitial silicate glass, minor orthoclase, and minor biotite (Fig. 6a). The chemical composition of the glass was highly heterogeneous and the transition from glass to orthoclase appeared to have happened locally (Table 3). Glass areas with distinct composition from orthoclase appeared to be mainly influenced by closely associated solids. For example, near (< 5 μm) the surface
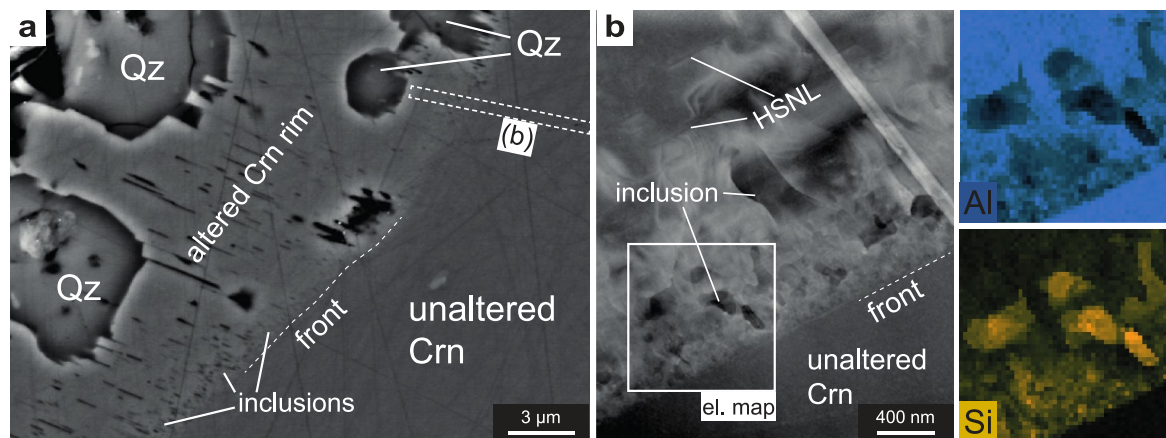
Fig. 7 Investigations on the Si reaction rim in natural Crn from Setup 5 (run 29). **a** The altered Crn rim (see Figure 6b for overview) shows an accumulation of nanometer sized inclusions along reaction front (or at the contact with unaltered Crn, marked with dashed white line; BSE image). Numerous larger Qz grains are located inside the rim. **b** TEM investigations along the contact between reaction front and unaltered Crn single crystal (indicated in **a**), HAADF (TEM) image displays parallel oriented HSNL and a high concentration of nano-inclusion and lattice defects. TEM EDS element map- pings of Al (upper right) and Si (lower right) show that the inclusions contain high amounts of Si and are completely depleted in Al. The inclusions tend to enlarge with increasing distance to the front

Table 4 Compositional profile C-D (in oxide wt%, 1 analysis point per 4 µm) through an Si-rich reaction rim in a natural corundum single crystal in runs 29; 690 ℃; 0.48 Gpa (Fig. 5) unreacted corundum areas in *italic* (WDS results EMP)

µm	0	4	8	12	16	20	24	28	32	36	D.L
SiO_2	*b.d*	*b.d*	*b.d*	*b.d*	*b.d*	*b.d*	*b.d*	4.14	0.70	2.24	0.06
Al_2O_3	*100.04*	*99.58*	*100.48*	*100.51*	*99.79*	*100.85*	*100.54*	99.33	99.83	96.87	0.15
Fe_2O_3	*0.08*	*0.06*	*0.05*	*0.07*	*0.07*	*0.06*	*0.07*	0.25	0.93	0.96	0.04
K_2O	*b.d*	*b.d*	*b.d*	*b.d*	*b.d*	*b.d*	*b.d*	b.d	b.d	0.245	0.11
Total	*100.12*	*99.64*	*100.53*	*100.58*	*99.86*	*100.91*	*100.61*	103.72	101.46	100.31	–

Single point measurements in corundum reaction rims				D.L
SiO_2	0.65	1.85	0.21	0.68	0.01
Al_2O_3	98.44	95.80	95.82	99.27	0.01
Fe_2O_3	0.80	0.62	0.84	0.85	0.01
K_2O	b.d	b.d	b.d	b.d	0.11
Total	99.89	98.27	96.87	100.80	–

of corundum single grains, the glass was enriched in SiO_2 and depleted in Al_2O_3 and newly grown quartz was commonly found associated with this Si-rich glass, whereas near quartz grains the glass composition showed the opposite chemical trend with Si depletion and Al enrichment (Fig. 6a, Table 3). No sillimanite was produced, instead additional solid products consisted of thin plates of corundum (< 1 µm width, < 3 µm in diameter) found dispersed in the silicate glass and occasionally in direct contact with quartz (Fig. 6a, Online Resource 10a, b). Biotite was found as < 0.5 µm thin plates, too small for quantitative chemical analysis.

The silicate glass was commonly associated with the corundum single crystals and appeared to have accumulated around the single crystals during the experiment. The corundum surface and cracks within the grains displayed reaction rims strongly resembling the altered margins of run products from setup 1 at low pH (Fig. 6, compare with Fig. 5). Unlike in setup 1, the outer surfaces of the rims from setup 5 in some places show a structure composed of parallel oriented discreet grains, which looks similar to epitaxial growth in a supersaturated system (Fig. 6b and 7a, for detailed discussion see Schultze et al. 2021). This is likely due to alumina being released as a result of the breakdown of muscovite in this setup. We observe both dissolution of the corundum single crystals with associated reaction rim formation (along cracks and phase boundaries, see Fig. 6), while locally corundum plates precipitate in the glass and potentially also epitaxially onto the attacked corundum surface. The reaction rims were enriched in SiO_2 (up to 4 wt%) compared to the non-altered corundum (< 0.1 wt%) and the highest concentrations in the rim were measured along the

reaction front (Si map in Fig. 6b, Table 4). An element profile *C-D* through the reaction front (Fig. 6b, Table 4) with additional single point measurements along the reaction rim shows that iron is enriched in the reaction rims (up to 1 wt% Fe_2O_3) compared with the unaltered corundum. This is the opposite trend as observed in reaction rims of setup 1 experiments, which are depleted in Fe (Fig. 2c, Table 4). Also, in contrast to products of setup 1, quartz inclusions are more abundant along the reaction rims in run 29 (Figs. 6b, 7). Natural single crystals differed from synthetic ones in that their reaction rims were generally wider (up to 20 µm), whereas the rims along synthetic grains were less than 10 µm wide. The polished basal plane of synthetic grains showed no visible alteration features.

TEM investigations revealed that the reaction rims contain Si-rich parallel oriented HSNL along (0001) planes (Fig. 7a, b). Due to the almost parallel position of the TEM foil to these planar rim features, the HSNL are poorly visible in Fig. 7b. In addition to nano-layers, numerous kidney-shaped, silica rich inclusions, the smallest of < 50 nm and the largest of just under 1 µm size, were observed in the foremost front of the reaction rim (Fig. 7b). Accounting for the considerable increase in Si along the reaction front, these inclusions likely represent the origin of the larger quartz grains that precipitated in the rim (Figs. 6b, 7a).

Discussion

The experiments presented in this study were conducted well inside the stability field of kyanite or sillimanite (see Table 1) according to experimental studies (e.g., Holdaway 1971; Pattison 2001), internally consistent thermodynamic data sets (Holland and Powell 2011), as well as according to studies that combined several approaches (Holdaway and Mukhopadhyay 1993; Pattison 2001). Aqueous fluid was either added or provided by dehydrating phyllosilicates in all runs in order to assure sufficiently high reaction rates. However, no coronas or precipitates of any Al_2SiO_5 polymorphs formed, instead dissolution- and precipitation-features of quartz and corundum were observed. This implies that aluminium silicate formation was not thwarted by slow kinetics and insufficient experimental run times but that the reaction pathway is obstructed. Comparison between the results of the different experimental approaches provides crucial information about the mechanisms controlling or obstructing the corona-forming reactions, as discussed in the following.

Corona formation in the system ASH (± X)

In pure water plus silica experiments (setup 1), a porous quartz coating formed on corundum single crystals. Underneath this coating, corundum dissolution appeared to be predominantly bound to the corundum-quartz phase boundary. Low dissolution rates of corundum and thus lack of Al_2O_3 saturation in the fluid with respect to kyanite (Beitter et al. 2008) could have hindered the nucleation of this phase. The higher corundum solubility in experiments with low pH (HCl or BH_3O_3 added, Fig. 1), as evidenced by intensified etch pit formation on the corundum surface, on the other hand, did not result in the formation of any Al_2SiO_5 polymorphs either.

One other possible factor inhibiting the precipitation of Al_2SiO_5 polymorphs may be their low nucleation rates. To test this, kyanite seeds were used in setup 2 (Table 1) and in other setups (Schultze et al. 2021) but no evidence of kyanite growth at the expense of corundum was observed, which seems to imply that not only the nucleation of kyanite, but also its growth in aqueous fluid is obstructed in the presented experiments. The formation of quartz + corundum or any other phase seems to be favored over the precipitation of kyanite, even when seed crystals provide a way to bypass the nucleation barrier.

The intense dissolution of corundum in experiments containing additional K^+, Na^+, Ca^{2+}, Mg^{2+}, or NH_4^+ (setup 3) is promoted by the precipitation of Al-bearing products. The net dissolution of Al_2O_3 is not controlled by the solubility of the pure phase in the fluid but rather by the amount of precipitated product. Therefore, the amounts of additional cations in the solution directly influences the amount of dissolving Al. Coronas of buddingtonite (ca. 100 µm wide, run 26) and clinochlore (ca. 10 µm wide, run 27) formed readily around corundum in our experiments (Online Resource 8). This clearly shows that corundum is in fact a suitable and compliant reactant for corona growth processes and that the generally low Al solubility in metamorphic fluids does not control the nucleation and crystal-growth processes. However, all but one experiments in setup 3 showed substantially less dissolution and precipitation along the corundum basal plane than on any other crystal face indicating passivated dissolution behavior in $[0001]_{Crn}$.

The experiment conducted with baddeleyite instead of corundum (setup 4) was identical to the experiments in setup 1 regarding the fluid composition. Despite the similarities of both systems (low solubility of the oxides, orthosilicate products, no topotactic replacement possible), a zircon corona formed after only 3 weeks of experiment by interaction of the baddeleyite surface with the quartz saturated fluid. The tendency of quartz saturated aqueous fluid to produce polymerized silica structures did not prevent the formation of zircon. TEM investigations found no hydrosilicate nanostructures comparable with HSNL along the interface of zircon and baddeleyite or within the dissolving baddeleyite, which implies spontaneous and direct zircon precipitation at the baddeleyite surface. Reasons for the opposing nucleation behavior of zircon and Al_2SiO_5 polymorphs at

nearly identical conditions, could be in part explained by differences in their molecular structure. Zr-O bond length in both baddeleyite (Zr^{VII}) and zircon (Zr^{VIII}) are on average ~ 2.20 Å, where Al-O bonds in corundum (Al^{VI}) and the three Al_2SiO_5 polymorphs (Al^{IV}, Al^V, Al^{VI}) are on average ~ 1.87 Å. Compounds with lower coordination numbers and shorter bond length require higher energy in order to transform.

Dehydration reactions in muscovite (setup 5) are known to generate all three Al_2SiO_5 polymorphs in metamorphic rocks (e.g., García-Casco et al. 1993; Sanchez-Navas 1999). The approach of run 29 was to simulate these natural processes, but no sillimanite was found among the products of decomposed muscovite (glass, orthoclase, quartz, corundum). Instead, fine grained corundum plates were found associated with the heterogeneous glass and quartz precipitated in direct contact with the large corundum single crystals or epitactically grown onto their reaction rims (Fig. 6). Chemical heterogeneities in a melt phase produced during dehydration reactions in pelitic rocks have also been reported, suggesting that SiO_2-undersaturated domains (with respect to quartz) could allow corundum to grow even in globally quartz saturated experiments (Kato et al. 2011). However, in run 29, abundant quartz and corundum growth was observed in Al-rich (e.g., on and in corundum) and Si-rich domains (Si rich glass or near quartz), respectively (Online Resource 10). This experiment shows that the dehydration of muscovite alone does not suffice to trigger the formation of the Al_2SiO_5 polymorphs (e.g., Huang and Wyllie 1974).

In summary, it can be concluded that experimental corona formation on corundum in general is not impeded by by a lack of reactivity of corundum because buddingtonite and clinochlore coronas form readily under the fluid and *P–T* conditions used in this study. The experiments, which produced zircon coronas around baddeleyite, on the other hand, show that additional cations in the fluid are not necessary to form a corona and that coronas of the orthosilicate of the substrate material are not inherently unfavorable. The observation that the kyanite and sillimanite formation was never observed in our experiments despite being thermodynamic equilibrium phases under the respective conditions, suggests that the obstruction in the formation of aluminum silicate coronas is related to the product side of the process, rather than the reactant side.

Silicate reaction rim formation on corundum

Three fundamentally different experimental approaches in setup 1 and 5 have shown that the interaction of corundum with silica provided by aqueous fluid or silicate melt, results in the formation of reaction rims along the corundum surface and into the grains. These rims are characterized by nanometer wide, HSNL distributed parallel to {0001} lattice planes of the corundum (Figs. 2, 6, 7). Even when the opportunity for corona formation was given (e.g., with precipitation of orthoclase in setup 5), reaction rims formed along corundum single crystal surfaces instead. The formation of these rims may, therefore, be responsible for impeding the formation of an aluminium silicate corona. The reaction rims documented in setup 1 and 5 experiments are caused by the dissolution or alteration of corundum. Corundum and silica-rich fluid (setup 1) or silicate melt (setup 5) interacted and display clear dissolution features along the corundum surface (rounded grains, etch pits, alteration along cracks and fluid trails, Figs.1, 2, 5, 6, Online Resource 3). The reaction rims formed in our experiments, strongly resemble fluid-mediated diffusion profiles or dissolution-reprecipitation features as known from literature (Putnis 2002; Putnis and Mezger 2004; Harlov et al. 2005; Putnis and Putnis 2007; Putnis and Austrheim 2010). It is therefore concluded that those rims form during the dissolution of corundum, which is coupled with the alteration of the grain due to silica influx into the corundum lattice (Figs. 1, 4). A crucial difference between setups 1 and 5 is that the outer perimeter of the rims in setup 5 show features that can be interpreted as epitaxial growth of corundum on corundum (Figs. 6 and 7), which was not observed in setup 1 (Figs. 1, 2, and 3). It therefore seems that the corundum grains in setup 5 may have experienced net growth during the experiment due to alumina released by the breakdown of muscovite. This is not possible in setup 1, which does not contain alumina-bearing phases other than corundum. However, net growth of corundum is not possible in hairline cracks, even in setup 5 (Fig. 5), unless they experienced significant opening. If such cracks had opened, which seems unlikely under hydrostatic pressure as in our experiments, the two parts of the crystal should show slightly different orientations, for which there is no indication in any of the cases observed by us. This suggests that, although additional precipitation may take place in setup 5, there is also a component of diffusion or dissolution-reprecipitation involved, which is similar to setup 1.

In order to get a complete picture of the dissolution processes involved in the reaction rim formation we discuss both surface features (etch pits etc.) and subsurface features (inside the altered corundum) in the following.

Surface features

Experiments with pH neutral aqueous fluid and silica showed a dissolution pattern on corundum that was mainly controlled by fluid pathways through the porous or incomplete quartz cover encasing the corundum crystals. However, with increasing corundum solubility (setups 1 and 3), dissolution features of the corundum became increasingly controlled by crystallographic orientation of the corundum, and

less by the quartz cover. Dissolution faces formed mainly in {10–12} and occasionally {-1014}, in agreement with theoretical dissolution models and experimental observations (Siesmayer et al. 1975; Smirnov et al. 1981) (Fig. 1c, d). The basal plane of corundum is free of etch pits and generally corona-free after weeks of experiment and appears to show a strong resistance to dissolution (Fig. 1b, c, d). Literature data suggests slow dissolution along [0001] but not completely passive behavior (Smirnov et al. 1981). After several weeks of interaction with acidic, quartz saturated fluid, a < 1 µm wide, silica-enriched layer is found on the basal plane of synthetic corundum grains (Online Resource 3). Shallow etch pits merely consist of areas where this layer was removed. This suggests that dissolution in [0001] is at least partly inhibited or passivated by the silica-enriched layer. In Schultze et al. (2021) we showed that corundum plates precipitating from quartz saturated fluids in experiments have a disproportionately large pinacoid {0001}, indicating extremely slow or obstructed growth perpendicular to {0001}. We conclude that the passivation in growth and dissolution behavior is most likely caused by hydrosilicate coating on the basal planes (Online Resource 3) that are exposed to the fluid, and that the coating is structurally similar to the HSNL found inside corundum (compare Suchanek and Garcés 2010). However, this proposed surface coating can only be observed but not quantified in situ with any method currently at our disposal.

Diffusion of Si into corundum

We interpret the several tens of micrometers wide silicon-enriched reaction rims (setup 1 and 5) to represent the result of introduction of chemical components from the fluid into the corundum single crystals via diffusion.

The redistribution of Fe trace concentrations along the reaction rim displays a typical diffusion pattern and depends on the availability of Fe during interaction of fluid or melt with the single crystal (Fig. 2c, Table 4). In setup 1, the reaction rims are depleted in Fe because the attacking agent (aqueous HCl + silica) was Fe-free, whereas in setup 5, higher Fe contents are measured in the reacted corundum compared with non-altered areas due to FeO contents of around 1.5 wt% in the muscovite starting material (compare Table 2, Table 4).

The Si and Al concentration profiles (e.g., Fig. 2), on the other hand, are somewhat unexpected in that they do not seem to follow Fick's law where concentration profiles of the diffusing components should resemble monotonically increasing or decreasing functions whose shape and slope depend on the chemical gradient between the reactants and elapsed time of interaction (Ganguly 2002; Abart et al. 2004; Harlov et al. 2005). The Si concentration profile in reacted corundum displays a distinct maximum content in the sharp

contact of reaction rim and unaltered single crystal (Fig. 2c, Tables 2, 4). A complementary pattern is observed in the Al distribution along the reaction rim, with a minimum Al concentration at the reaction front. Aluminium and Si diffuse against their concentration gradient within the reaction rim. Similar concentration profiles are known from uphill diffusion processes in various physicochemical systems (Ganguly 2002; Kohn and Penniston-Dorland 2017; Zhang 2008). In multi-component systems, the diffusion flux of a single component is not solely controlled by its own concentration and chemical potential gradient, but is influenced by the other diffusing components (coupled diffusion), which can result in uphill diffusion of certain components with respect to their concentration gradient in order to minimize the thermodynamic potential of the system (e.g., Krishna 2015; Yund and Snow 1989). Systems with fewer diffusive components, specifically binary systems, experience uphill diffusion when the host phase undergoes spinodal decomposition (e.g., Petrishcheva and Abart 2012; Zhang 2008). Furthermore, uphill diffusion is also observed in nanoporous solids interacting with fluid (e.g., Lauerer et al. 2015; Krishna 2019). All three of these scenarios might play a more or less pronounced role in the formation of Si-rich reaction rims in corundum.

Silicate systems often display coupled interdiffusion including charge balancing ion pairs when Si and Al are exchanged (such as the well-known coupled substitution $NaSiCa_{-1}Al_{-1}$ in plagioclase, e.g., Yund and Snow 1989). In corundum the substitution mechanism of Al^{3+} with Si^{4+} requires charge balance much like the incorporation of Ti^{4+}, the most prominent other tetravalent trace element in corundum. In high concentrations, TiO_2 forms rutile needles in the basal plane of its host, which have been interpreted to be either exsolution features at lower temperatures (e.g., Emmett and Douthit 1993) or a feature of syngenetic epitaxial coprecipitation during corundum growth (Palke and Breeding 2017). In corundum, Ti replaces Al along three different substitutions, (1) $Al^{3+} <=> Ti^{4+} + 0.5O^{2-}$, (2) $2Al^{3+} <=> Ti^{4+} + Fe^{2+}$ (or other divalent trace elements), and (3) $Al^{3+} <=> Ti^{3+}$ (Nassau 1981). Since a reduction of Si^{4+} in our experiments is impossible and the increase in Si along the diffusion rims coincides with either an increase or decrease in Fe in different experiments (Fig. 2c, Table 4), the substitution of Al^{3+} with Si^{4+} more likely involves the formation of cation vacancies, possibly in combination with charge balancing protons. This might explain why the Si diffusion rims are pronounced in experiments with low pH compared to pH-neutral settings. Proton diffusion rates are generally fast and H^+ tends to influence the flux pattern of other (slower) components, which can lead to uphill diffusion profiles of these components in the infused medium (Krishna 2015). Since we also observed Si-enriched rims in corundum attacked by alkaline fluid or melt (setup 5), it

cannot be determined definitively whether H^+ plays a similar role in our low pH experiments. However, the elevated Al solubility in acidic or alkaline compared to neutral environments (e.g., Carroll-Webb and Walther 1988; Wohlers and Manning 2009), clearly enhances the diffusive exchange with Si.

Formation and influence of hydro-silicate nano-layers (HSNL)

Admittedly, the substitution mechanism of $Al \rightarrow Si$ in corundum is poorly understood and, to our knowledge, this study is the first one reporting pronounced Si diffusion into corundum. However, trace concentrations of Si in natural corundum are generally ≤ 700 ppm according to the scarce literature data that is available on that matter (Harlow and Bender 2013; Sutherland et al. 2014). Concentrations above 700 ppm and up to 5000 ppm as measured in the reaction rims of our samples are likely above the solubility limits of Si in corundum. Such concentrations have been reported only from rubies that have been influenced by skarn formation processes or metasomatic alteration in the Mogok metamorphic belt of Myanmar by Harlow and Bender (2013), who proposed "fine-scale inclusions, not visible by optical or most electron microscopy" as possible source of the unusually high Si content. The HSNL found in the reaction rims in our samples correspond precisely to this description. If we conclude that the capacity of corundum to dissolve Si is exceeded within the reaction rim, then the formation process of HSNL displays aspects of spinodal decomposition (e.g., Petrishcheva et al. 2020; Wang et al. 2022; Weinbruch et al. 2003). In Fig. 3a a strongly Si enriched reaction front without discernible HSNL is closely followed by an area of evenly distributed, strictly oriented HSNL. The high concentration of Si at the reaction front creates an area of thermodynamic instability in the corundum leading to the spontaneous formation of metastable HSNL, a transient phase that utilizes crystallographic features of the corundum host to its energetic advantage. In doing so, the system circumvents the nucleation activation energy necessary to produce the stable Al_2SiO_5 polymorph (Alert et al. 2016; Petrishcheva and Abart 2012).

The corundum basal plane is structurally similar to the octahedral layer of dioctahedral phyllosilicates (kaolinite, pyrophyllite, etc.) and inserting a tetrahedral silica layer parallel to (0001) is possible if at least two octahedral layers are removed from corundum (Fig. 4). Silicon replaces Al approximately in a ratio of 1:2 (Fig. 3c) and a substitution of two octahedral layers would result in a single tetrahedral-octahedral layer pair and corresponding lattice gap as known from e.g., kaolinite (Fig. 4). HRTEM images in combination with TEM-EDS line scans (Fig. 3c) suggest a substitution mechanism of two Al-octahedral layers: $2Al^{3+} \rightarrow Si^{4+} + 2H^+$

or three Al-octahedral layers: $3Al^{3+} \rightarrow 2Si^{4+} + H^+$ (Fig. 4). Nano-structures larger than silica double layers were not found, which is probably due to the mismatch between the corundum host and the nano-layers. The latter do not have enough space in $[0001]_{Crn}$ to develop a proper dioctahedral phyllosilicate structure, since e.g., the distance between two neighboring Al-octahedral layers in pyrophyllite is 0.1 nm larger than that of the corresponding layers in corundum. Considering that unseeded kyanite corona formation is achieved at experimental pressures of ≥ 2 GPa (Harlov and Milke 2002), one could speculate HSNL are only able to form and thereby suppress kyanite formation only at pressures < 2 GPa, because the structural mismatch in [0001] becomes too large at higher pressure. The formation of HSNL by the described substitution mechanisms creates nanometer wide gaps or nano-porosity in the corundum lattice (Fig. 4) similar to porosity that has been described from dissolution-reprecipitation processes in other chemical systems (Walker et al. 1995; Harlov et al. 2005; Putnis and Putnis 2007). Once formed, the HSNL allow for an accelerated and anisotropic mass transfer into and out of the corundum. The modified mass transfer enhances the Si transport through the rim and towards the reaction front, explaining the sharp profile of Si with a maximum concentration at the reaction front (Fig. 2c, Tables 2, 4).

Accumulation and annealing of HSNL

With increasing distance to the front, the HSNL are accumulated along discrete layers within otherwise HSNL-free corundum. This Ostwald ripening and coarsening between the discerning phases is also inherent to spinodal decomposition (e.g. Zhang 2008). An important distinction between the process observed in Si-infused corundum and well-known petrological systems undergoing spinodal decomposition, e.g. pyroxenes and feldspars (e.g. Petrishcheva et al. 2020; Wang et al. 2022), however, is the crystallographic mismatch between corundum and potential hydrosilicate-phases (e.g. kaolinite, pyrophyllite, etc.) that could form within corundum and attaching to $\{0001\}_{Crn}$. The HSNL were only observed as single or double Si-tetrahedral layers replacing Al-octahedral layers. No complete unit cells of either kaolinite, pyrophyllite etc. were found, which is likely due to this mismatch. The occurrence of HSNL must have an influence on the local chemical potential of both Si and Al and could locally lower the chemical potential of Si. This would explain the continuing intake of Si into an effectively Si supersaturated corundum, which in turn may result in the uphill diffusion pattern of Si along the entire reaction rim. However, the HSNL also induce nanoporosity into the reaction rim, which may play a more pronounced role in the concentration profile of Si and Al in the reaction rim.

Newly precipitated quartz grains are found frequently inside the reaction rims, often specifically located along the diffusion front where otherwise the Si maximum is measured (Figs. 2, 7). These inclusions are interpreted as a supersaturation of silica with respect to the formation capacity of HSNL in the corundum. They are probably a result of the self-enhanced Si influx caused by the nano-layer formation. Behind the first 500 nm, larger but fewer quartz grains of up to 10 μm in diameter suggest continuous reorganization of excess silica within the reaction rim and Ostwald ripening processes (Figs. 2, 5, 6). The disparity of quartz inclusions in different experiments likely reflects the different Si diffusion rates caused by different attacking agents in setup 1 and 5 (fluid and liquid/melt). Cracks parallel to (0001) of reacted corundum in setup 5 could suggest that the high Si content results in a volume expansion. Fracturing of the reaction rim further increases the permeability for fluids and liquids (Figs. 6, 7).

HSNL bearing reaction rims along permeable features in corundum (preexisting inclusion trails or cracks, Fig. 5a) appear to anneal with prolonged experimental duration of over two weeks resulting in quartz and fluid filled inclusions in HNSL-free corundum (Fig. 5b, c). This implies that the HSNL is no precursor phase on the way to aluminium silicate Al_2SiO_5 formation, as transient metastable phases in other systems often are (e.g. Kutzschbach et al. 2017). On the contrary, it is more likely that due to the presence of HSNL in an environment of Al and Si ovsupersaturation (this study and Schultze et al. 2021), the metastability of quartz and corundum is both initially favored over aluminium silicate precipitation as well as during the HSNL retreat and coarsening of the bulk phases.

## Implications for aluminium silicate formation and outlook

A conclusive reason why quartz forms inside corundum instead of the thermodynamically favorable Al_2SiO_5 polymorph, has yet to be found. However, one could argue that a tetrahedral silica-layer is structurally more closely related to the silica network in quartz than to the isolated position of single silica tetrahedra in the aluminium silicates and thus less reorganization of atomic bonds is required for quartz nucleation. Additionally, free energy barriers for heterogenous nucleation are reduced along metastable crystallographic "defects" (Binder and Fratzl 2001), which the HSNL constitute. Quartz inclusions in corundum from Proterozoic gneisses in the Bamble sector in Norway (Kihle et al. 2010) support the idea that once formed the coexistence of quartz and corundum can persist essentially indefinitely.

This type of thermodynamic corundum-quartz-conundrum is known from other systems. Despite large volumes of natural dolomite occurrences (e.g. the Dolomite Mountains) evidently produced by inorganic precipitation from fluid, all attempts at synthesizing dolomite from dolomite supersaturated fluid had long been unsuccessful, which became known as the "dolomite problem". Just recently Kim et al. (2023) uncovered that the dolomite system is governed by a growth inhibition resulting from a critical density of disordered Mg-Ca areas in the initial nucleation products. This inhibition can only be overcome by periodically fluctuating the fluid from dolomite supersaturation to undersaturation, whereby disordered areas are preferentially dissolved within the nuclei during undersaturated periods thus allowing the remaining ordered areas to grow under supersaturated conditions. A previous experiment at constant dolomite supersaturation did not produce any dolomite over a runtime of 32 years (Land 1998), demonstrating that nanometric crystal structures can hold entire chemical systems "hostage" against thermodynamic predictions. Since our experiments in the ASH system require higher *P–T*-conditions than dolomite synthesis, fluctuating fluid pH or composition as well as fluctuations in P and T is comparably difficult to achieve.

We cannot conclusively answer the question why the Al_2O_3 polymorphs have proven so difficult to produce in experiments but form so readily in nature at this point. However, our research presented here suggests a hypothesis, which may be tested in the future. It appears that the transient nano-layer phase (HSNL) impedes the nucleation of aluminium silicates by redirecting the reaction pathway toward the metastable association corundum+quartz. We propose that the reorganization of the phyllosilicate structure of the HSNL into the silica tetrahedral network of quartz requires less activation energy than reorganization into the orthosilicates (or nesosilicates) kyanite or sillimanite, with their isolated silica tetrahedra. The reason for the difference in activation energy may be found in the number of strong bonds between corner-sharing tetrahedra that need to be broken. Silica tetrahedra are among the strongest bonds in most silicates. In the tetrahedral sheets of phyllosilicates, each Si tetrahedron is connected to three other silica or alumina tetrahedra, meaning that to isolate a single Si tetrahedron (to get the configuration found in orthosilicates), three Si–O or Al-O of the adjacent tetrahedra need to be broken. To form the tetrahedral framework of quartz from a phyllosilicate requires more breaking of bonds in the octahedral layers but fewer of the shorter and stronger tetrahedral bonds are broken. Whether or not this effect is sufficient to effectively divert the reaction pathway away from aluminium silicate formation and toward quartz formation cannot effectively be investigated experimentally but could be tested with carefully designed molecular dynamics calculations. However, due to the complexity of the system, this is a major undertaking.

The failure of experiments to replicate nature is likely related to some of the many aspects of natural systems that we cannot or at least do not usually replicate in the
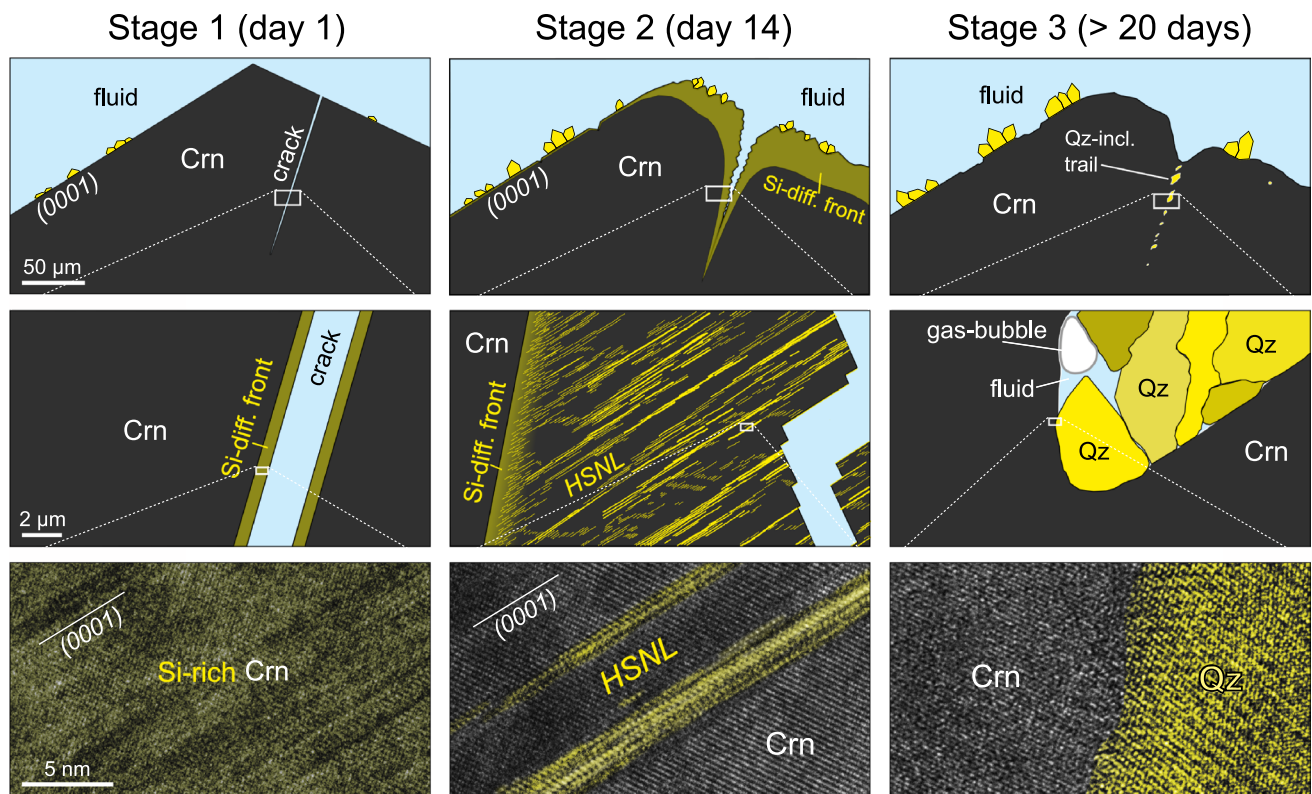
Fig. 8 Stage 1 diffusion: Silicon from the quartz saturated fluid or melt enters the corundum lattice via bulk diffusion while Al counter-diffuses out and gets dissolved in the corundum undersaturated fluid. This proceeds for a few tens of nanometers until the solubility limit of Si in corundum is reached. Because Al actively diffuses out of the corundum into the Al undersaturated (with respect to corundum) fluid, Si counter-diffusion into the corundum is enhanced by the need for charge balance and due to the structural holes left by the missing Al ions. This allows the Si concentration in corundum to rise past the normal Si solubility limit in corundum. **Stage 2** condensation: At some point after this solubility limit is exceeded, the HSNL nucleate parallel to the basal plane of the host corundum and take up the excess Si. The structure of the nano-layers is relatively open within the basal plane compared to corundum, thus providing a faster transport pathway for the exchange of Si and Al than bulk diffusion. The formation of HSNL, therefore, increases the influx of Si and pushes the reaction front further into the corundum. This mechanism is effective for diffusion in the basal plane (i.e., perpendicular to [0001]) of corundum but absent in any other directions, especially along <0001>. The HSNL even block diffusion into the {0001} faces. The increasing formation of HSNL leads to stress and strain due to the lattice mismatch between the HSNL and the host corundum. As a result, the HSNL condense from many single layers to fewer multi-layered structures (Ostwald ripening) to reduce stress. This stage was prominently observed after roughly 2 weeks in rims of up to 100 μm width perpendicular to [0001] of corundum. However, the condensation of HSNL cannot proceed indefinitely because they are not stable as a bulk phase and require stabilization by some strain imparted by the mismatch with the corundum host. **Stage 3** annealing: As the HSNL condense further, bulk thermodynamics overcome the stabilizing effect of the HSNL-corundum interface. This should lead to the formation of aluminium silicates but instead leads to the formation of quartz inclusions as a metastable assemblage with the surrounding corundum. After about 20 weeks, most HSNL have been converted to quartz in Si-poor corundum and the diffusion of Si into the corundum grains seems to terminate. The fact that no further Si diffuses into the corundum is probably due to the fluid nearing corundum saturation, which means that Al no longer has a gradient against which to diffuse out of the corundum. Counter-diffusion of Al was a prerequisite to allow the intense diffusion of Si into the corundum during stages 1 and 2

laboratory. For future attempts to experimentally nucleate and grow Al_2SiO_5 polymorphs it may be worth exploring a similar saturation cycling method, as has been successfully applied to dolomite formation (Kim et al. 2023). It has also been noted in the past that biotite may act as a more promising catalyst or precursor phase for Al_2SiO_5 polymorphs then muscovite (e.g., Yardley 1977; Foster 1991) and, therefore, experiments similar to ours but additionally containing biotite might provide additional insights. Another avenue that may be worth exploring is that of open systems where the concentration of Si and Al in solution can be more freely manipulated than in closed systems, which rely on mineral phase saturation. Such a study would likely require substantial development work on a new experimental apparatus, which may prove useful for a wide range of open questions in metamorphic petrology.

Conclusions

Neither the interaction of corundum with quartz saturated fluid (setup 1), nor the interaction of corundum with silicate melt (setup 5) seems to be able to produce aluminium silicate coronas in closed systems such as the presented hydrothermal and piston cylinder experiments. Comparison with the spontaneous formation of coronas of other silicates around corundum as well as that of zircon around baddeleyite indicates that the limiting factor for experimentally producing aluminium silicate coronas cannot be dissolution or transport kinetics. Instead, both nucleation and growth of Al_2SiO_5 polymorphs seem to be obstructed by factors, which likely require a substantially different experimental design to overcome.

Instead of aluminium silicate corona growth, Si-diffusion into corundum host grains produced complex reaction rims in our samples, which show a characteristic development over several weeks of experimental time. The formation of these rims is coupled to corundum dissolution in the surrounding quartz saturated fluid/melt and appears to proceed in three overlapping stages, schematically shown in Fig. 8 at three different scales each.

Our findings indicate that the presence of aqueous fluid does not necessarily in and of itself promote the reaction of corundum and silica to the stable Al_2SiO_5 polymorph, or the formation of the phase assemblage predicted by bulk thermodynamics in general. Natural observations of the metastable assemblage corundum + quartz can therefore not unambiguously be interpreted as an indicator for "dry" or fluid-absent formation conditions. On the contrary, processes observed in experiments of this and a previous study (Schultze et al. 2021) suggest that an increased water activity can sustain and favor the metastability of corundum and quartz. Natural quartz inclusions in corundum might very well stem from an interaction of the corundum with quartz saturated aqueous fluid.

More broadly, the results presented in this study suggest that "hidden phases" such as the HSNL can, under certain circumstances, divert a chemical system's path to thermodynamic equilibrium in the direction of a persistent metastable state. The nanoscopic and transient nature of the responsible phases makes them difficult to identify in experimental and especially in natural systems, which means that they may be more common and more relevant in natural processes than we are currently aware. If the phenomena described here are not unique to the ASH system, which we consider likely, then mineral reactions that apparently deviate from predictions based on bulk thermodynamics are certainly worth closer investigation in the future.

References

Abart R, Kunze K, Milke R, Sperb R, Heinrich W (2004) Silicon and oxygen self diffusion in enstatite polycrystals: the Milke et al. (2001) rim growth experiments revisited. Contrib Mineral Petrol 147:633–646. https://doi.org/10.1007/s00410-004-0596-9

Alert R, Tierno P, Casademunt J (2016) Formation of metastable phases by spinodal decomposition. Nat Commun 7:13067. https://doi.org/10.1038/ncomms13067

Althaus E (1967) The triple point andalusite-sillimanite-kyanite an experimental and petrologic study. Contrib Mineral Petrol 16:29–44. https://doi.org/10.1007/BF00371606

Anderson GM, Burnham CW (1967) Reactions of quartz and corundum with aqueous chloride and hydroxide solutions at high temperatures and pressures. Am J Sci 265:12–27. https://doi.org/10.2475/ajs.265.1.12

Anovitz LM, Essene EJ, Metz GW et al (1993) Heat capacity and phase equilibria of almandine, $Fe_3Al_2Si_3O_{12}$. Geochim Cosmochim Acta 57:4191–4204. https://doi.org/10.1016/0016-7037(93)90315-N

Aramaki S, Roy R (1963) A new polymorph of Al_2SiO_5 and further studies in the system Al_2O_3-SiO_2-H_2O. Am Mineral 48:1322–1347

Becker KH, Cemic L, Langer KEOE (1983) Solubility of corundum in supercritical water. Geochim Cosmochim Acta 47:1573–1578. https://doi.org/10.1016/0016-7037(83)90183-7

Beitter T, Wagner T, Markl G (2008) Formation of kyanite-quartz veins of the Alpe Sponda, Central Alps, Switzerland: Implications for Al transport during regional metamorphism. Contrib to Mineral Petrol 156:689–707. https://doi.org/10.1007/s00410-008-0310-4

Binder K, Fratzl P (2001) Spinodal decomposition. In: Kostorz G (ed) Phase transformations in materials. Wiley, New York. https://doi.org/10.1002/352760264X.ch6

Burnham CW, Ryzhenko BN, Schitel D (1973) Water solubility of corundum at 500–800 °C and 6 kbar. Geochemistry Int 10:1374

Carr M, Fyfe WS (1960) Synthesis fields of some aluminium silicates. Geochim Cosmochim Acta 21:99–109

Carroll-Webb SA, Walther JV (1988) A surface complex reaction model for the pH-dependences of corundum and kaolinite

dissolution rates. Geochim Cosmochim Acta 52:2609–2623. https://doi.org/10.1016/0016-7037(88)90030-0

Day HW (1973) The high temperature stability of muscovite plus quartz. Am Mineral 58:255–262

Emmett JL, Douthit TR (1993) Heat treating the sapphires of Rock Creek, Montana. Gems Gemol 29:250–272. https://doi.org/10.5741/GEMS.29.4.250

Foster CT (1991) The role of biotite as a catalyst in reaction mechanisms that form sillimanite. Can Mineral 29:943–963

Ganguly J (2002) Diffusion kinetics in minerals: principles and applications to tectono-metamorphic processes. EMU Notes Mineral 4:271–309

García-Casco A, Sánchez-Navas A, Torres-Roldán L (1993) Disequilibrium decomposition and breakdown of muscovite in high P-T gneisses, Betic alpine belt (southern Spain). Am Mineral 78:158–177

Gottschalk M (1996) Internally consistent thermodynamic data for rock-forming minerals in the system SiO_2-TiO_2-Al_2O_3-Fe_2O_3-CaO-MgO-FeO-K_2O-Na_2O-H_2O-CO_2. Eur J Mineral 9:175–223. https://doi.org/10.1127/ejm/9/1/0175

Guiraud M, Kienast JR, Ouzegane K (1996) Corundum-quartz bearing assemblage in the Ihouhaounene area (In Ouzzal, Algeria). J Metamorph Geol 14:754–762. https://doi.org/10.1111/j.1525-1314.1996.00046.x

Harlov DE, Milke R (2002) Stability of corundum + quartz relative to kyanite and sillimanite at high temperature and pressure. Am Mineral 87:424–432. https://doi.org/10.2138/am-2002-0406

Harlov DE, Wirth R, Förster HJ (2005) An experimental study of dissolution-reprecipitation in fluorapatite: fluid infiltration and the formation of monazite. Contrib Mineral Petrol 150:268–286. https://doi.org/10.1007/s00410-005-0017-8

Harlov DE, Milke R, Gottschalk M (2008) Metastability of sillimanite relative to corundum and quartz in the kyanite stability field: Competition between stable and metastable reactions. Am Mineral 93:608–617. https://doi.org/10.2138/am.2008.2655

Harlow GE, Bender W (2013) A study of ruby (corundum) compositions from the Mogok Belt, Myanmar: searching for chemical fingerprints. Am Mineral 98:1120–1132. https://doi.org/10.2138/am.2013.4388

Holdaway MJ (1971) Stability of andalusite and the aluminum silicate phase diagram. Am J Sci 271:97–131. https://doi.org/10.2475/ajs.271.2.97

Holdaway MJ, Mukhopadhyay B (1993) A reevaluation of the stabilitv relations of andalusite: thermochemical data and phase diagram for the aluminum silicates. Am Mineral 78:298–315

Holland TJB, Powell R (2011) An improved and extended internally consistent thermodynamic dataset for phases of petrological interest, involving a new equation of state for solids. J Metamorph Geol 29:333–383. https://doi.org/10.1111/j.1525-1314.2010.00923.x

Huang WL, Wyllie PJ (1974) Melting relations of muscovite with quartz and sanidine in the K_2O-Al_2O_3-SiO_2-H_2O system to 30 kilobars and an outline of paragonite melting relations. Am J Sci 274:378–395. https://doi.org/10.2475/ajs.274.4.378

Kato M, Hiroi Y, Harlov DE et al (2011) Metastable corundum + quartz + andalusite association in pelitic granulite from the Kerala Khondalite Belt, southern India. J Mineral Petrol Sci 106:195–203. https://doi.org/10.2465/jmps.101116

Kerrick DM (1990) The Al_2SiO_5 polymorphs, vol 22. Mineralogical Society of America.

Kihle J, Harlov DE, Frigaard O, Jamtveit B (2010) Epitaxial quartz inclusions in corundum from a sapphirine-garnet boudin, Bamble Sector, SE Norway: SiO_2-Al_2O_3 miscibility at high P-T dry granulite facies conditions. J Metamorph Geol 28:769–784. https://doi.org/10.1111/j.1525-1314.2010.00891.x

Kim J, Kimura Y, Puchala B, Yamazaki T, Becker U, Sun W (2023) Dissolution enables dolomite crystalgrowth near ambient conditions. Science 382(6673):915–920

Kohn MJ, Penniston-Dorland SC (2017) Diffusion: obstacles and opportunities in petrochronology. Rev Mineralo Geochem. 83:103–152

Krishna R (2015) Uphill diffusion in multicomponent mixtures. Chem Soc Rev 44:2812–2836. https://doi.org/10.1039/C4CS00440J

Krishna R (2019) Diffusing uphill with James Clerk Maxwell and Josef Stefan. Chem Eng Sci 195:851–880. https://doi.org/10.1016/j.ces.2018.10.032

Kutzschbach M, Wunder B, Meixner A, Wirth R, Heinrich W, Franz G (2017) Jeremejevite as a precursor for olenitic tourmaline: consequences of non-classical crystallization pathways for composition, textures and B isotope patterns of tourmaline. Eur J of Min 29:239–255. https://doi.org/10.1127/ejm/2017/0029-2604

Land LS (1998) Failure to precipitate dolomite at 25 °c from dilute solution despite 1000-fold oversaturation after 32 years. Aq Geochem 4:361–368. https://doi.org/10.1023/A:1009688315854

Lauerer A, Binder T, Chmelik C, Miersemann E, Haase J, Ruthven DM, Kärger J (2015) Uphill diffusion and overshooting in the adsorption of binary mixtures in nanoporous solids. Nat Commun 6:7697. https://doi.org/10.1038/ncomms8697

Lucassen F, Dulski P, Abart R et al (2010) Redistribution of HFSE elements during rutile replacement by titanite. Contrib to Mineral Petrol 160:279–295. https://doi.org/10.1007/s00410-009-0477-3

Lucassen F, Franz G, Rhede D (2012a) Small-scale transport of trace elements Nb and Cr during growth of titanite: An experimental study at 600 °C, 0.4 GPa. Contrib to Mineral Petrol 164:987–997. https://doi.org/10.1007/s00410-012-0784-y

Lucassen F, Franz G, Wirth R et al (2012b) The morphology of the reaction front of the dissolution-precipitation reaction rutile + wollastonite = titanite in time series experiments at 600 °C/400 MPa. Am Mineral 97:828–839. https://doi.org/10.2138/am.2012.3742

Migdisov AA, Williams-Jones AE, van Hinsberg V, Salvi S (2011) An experimental study of the solubility of baddeleyite (ZrO_2) in fluoride-bearing solutions at elevated temperature. Geochim Cosmochim Acta 75:7426–7434. https://doi.org/10.1016/j.gca.2011.09.043

Milke R, Wiedenbeck M, Heinrich W (2001) Grain boundary diffusion of Si, Mg, and O in enstatite reaction rims: a SIMS study using isotopically doped reactants. Contrib to Mineral Petrol 142:15–26. https://doi.org/10.1007/s004100100277

Momma K, Izumi F (2011) VESTA 3 for three-dimensional visualization of crystal, volumetric and morphology data. J Appl Crystallogr 44:1272–1276. https://doi.org/10.1107/S0021889811038970

Mookherjee M, Keppler H, Manning CE (2014) Aluminum speciation in aqueous fluids at deep crustal pressure and temperature. Geochim Cosmochim Acta 133:128–141. https://doi.org/10.1016/j.gca.2014.02.016

Motoyoshi Y, Hensen BJ, Matsueda H (1990) Metastable growth of corundum adjacent to quartz in a spinel-bearing quartzite from the Archaean Napier Complex, Antarctica. J Metamorph Geol 8:125–130. https://doi.org/10.1111/j.1525-1314.1990.tb00459.x

Mouri H, Andreoli MAG, Kienast JR et al (2003) First occurrence of the rare "corundum + quartz" assemblage in the high-grade zone from the Namaqualand Metamorphic Complex, South Africa: evidence for higher-P, T metamorphism? Mineral Mag 67:1015–1021. https://doi.org/10.1180/0026461036750140

Nassau K (1981) Heat treating ruby and sapphire: technical aspects. Gems Gemol. 17:121–131

Palke AC, Breeding CM (2017) The origin of needle-like rutile inclusions in natural gem corundum: a combined EPMA, LA-ICP-MS, and nanoSIMS investigation. Am Mineral 102:1451–1461. https://doi.org/10.2138/am-2017-5965

Pattison DRM (2001) Instability of Al_2SiO_5 "triple-point" assemblages in muscovite plus biotite plus quartz-bearing metapelites, with implications. Am Mineral 86:1414–1422. https://doi.org/10.2138/am-2001-11-1210

Petrishcheva E, Abart R (2012) Exsolution by spinodal decomposition in multicomponent mineral solutions. Acta Mater 60(15):5481–5493. https://doi.org/10.1016/j.actamat.2012.07.006

Petrishcheva E, Tiede L, Schweinar K, Habler G, Li C, Gault B, Abart R (2020) Spinodal decomposition in alkali feldspar studied by atom probe tomography. Phys Chem Minerals 47:30. https://doi.org/10.1007/s00269-020-01097-4

Pokrovski GS, Schott J, Harrichoury JC, Sergeyev AS (1996) The stability of aluminum silicate complexes in acidic solutions from 25 to 150°C. Geochim Cosmochim Acta 60:2495–2501. https://doi.org/10.1016/0016-7037(96)00123-8

Putnis A (2002) Mineral replacement reactions: from macroscopic observations to microscopic mechanisms. Mineral Mag 66:689–708. https://doi.org/10.1180/0026461026650056

Putnis A, Austrheim H (2010) Fluid-induced processes: metasomatism and metamorphism. Geofluids 10:254–269. https://doi.org/10.1111/j.1468-8123.2010.00285.x

Putnis CV, Mezger K (2004) A mechanism of mineral replacement: Isotope tracing in the model system KCl-KBr-H_2O. Geochim Cosmochim Acta 68:2839–2848. https://doi.org/10.1016/j.gca.2003.12.009

Putnis A, Putnis CV (2007) The mechanism of reequilibration of solids in the presence of a fluid phase. J Solid State Chem 180:1783–1786. https://doi.org/10.1016/j.jssc.2007.03.023

Ragnarsdottir KV, Walther JV (1985) Experimental determination of corundum solubilities in pure water between 400–700°C and 1–3 kbar. Geochim Cosmochim Acta 48:159–176. https://doi.org/10.1016/0016-7037(85)90068-7

Roy DM (1954) Hydrothermal synthesis of andalusite. Am Mineral 39:140–143

Salvi S, Pokrovski GS, Schott J (1998) Experimental investigation of aluminum-silica aqueous complexing at 300°C. Chem Geol 151:51–67. https://doi.org/10.1016/S0009-2541(98)00070-9

Sanchez-Navas A (1999) Sequential kinetics of a muscovite-out reaction: a natural example. Am Mineral 84:1270–1286. https://doi.org/10.2138/am-1999-0905

Schilling F, Wunder B (2004) Temperature distribution in piston-cylinder assemblies: numerical simulations and laboratory experiments. Eur J Mineral 16:7–14. https://doi.org/10.1127/0935-1221/2004/0016-0007

Schultze DS, Wirth R, Wunder B, Loges A, Wilke M, Franz G (2021) Corundum-quartz metastability: the influence of a nanometer-sized phase on mineral equilibria in the system Al_2O_3–SiO_2–H_2O. Contrib Mineral Petrol 176:27. https://doi.org/10.1007/s00410-021-01786-5

Shaw RK, Arima M (1998) A corundum—quartz assemblage from the Eastern Ghats Granulite Belt, India: evidence for high P – T metamorphism? J Metamorph Geol 16:189–196. https://doi.org/10.1111/j.1525-1314.1998.00073.x

Siesmayer B, Heimann R, Franke W (1975) The dissolution forms of single crystal spheres. J Cryst Growth 28:157–161. https://doi.org/10.1016/0022-0248(75)90036-6

Smirnov AE, Urusovskaya AA, Govorkov VG, Berezhkova GV (1981) Thermochemical dissolution of corundum. J Mater Sci 16:1071–1080. https://doi.org/10.1007/BF00542754

Suchanek WL, Garcés JM (2010) Hydrothermal synthesis of novel alpha alumina nano-materials with controlled morphologies and high thermal stabilities. CrystEngComm 12:2996–3002. https://doi.org/10.1039/B927192A

Sutherland F, Zaw K, Meffre S et al (2014) Advances in trace element "Fingerprinting" of Gem Corundum, Ruby and Sapphire, Mogok Area, Myanmar. Minerals 5:61–79. https://doi.org/10.3390/min5010061

Tracy RJ, McLellan EL (1985) A natural example of the kinetic controls of compositional and textural equilibration. In: Thompson AB, Rubie DC (eds) Metamorphic reactions kinetics, textures and deformation. Springer, New York, pp 118–137

Wahl FM, Grim RE, Graf RB (1961) Phase transformation in silica-alumina mixtures as examined by continuous X-ray diffraction. Am Mineral 46:1064–1076

Walker FDL, Lee MR, Parsons I (1995) Micropores and microper-meable texture in alkali feldspars: geochemical and geophysical implications. Mineral Mag 59:505–534. https://doi.org/10.1180/minmag.1995.059.396.12

Walther JV (1997) Experimental determination and interpretation of the solubility of corundum in H_2O between 350 and 600°C from 0.5 to 2.2 kbar. Geochim Cosmochim Acta 61:4955–4964. https://doi.org/10.1016/S0016-7037(97)00282-2

Wang WJ, Gong DL, Wang HL, Ke YB, Qi L, Li SJ, Yang R, Hao YL (2022) Spinodal decomposition coupled with a continuous crystal ordering in a titanium alloy. Acta Materialia. https://doi.org/10.1016/j.actamat.2022.117969

Weinbruch S, Styrsa V, Müller WF (2003) Exsolution and coarsening in iron-free clinopyroxene during isothermal annealing. Geochim Cosmochim Acta 67:5071–5082. https://doi.org/10.1016/S0016-7037(03)00205-9

Whitney DL, Evans BW (2010) Abbreviations for names of rock-forming minerals. Am Mineral 95:185–187. https://doi.org/10.2138/am.2010.3371

Wirth R, Wunder B (2000) Characterization of OH-containing phases by TEM using electron energy-loss spectroscopy (EELS): clino-humite-OH, chondrodite-OH, phase A and the (F, OH)-solid solution series of topaz. J Trace and Microprobe Techniques 18:35–49

Wohlers A, Manning CE (2009) Solubility of corundum in aqueous KOH solutions at 700 °C and 1 GPa. Chem Geol 262:310–317. https://doi.org/10.1016/j.chemgeo.2009.01.025

Yardley BWD (1977) The nature and significance of the mechanism of sillimanite growth in the Connemara schists, Ireland. Contr Mineral and Petrol 65:53–58. https://doi.org/10.1007/BF00373570

Yardley BWD, Cleverley JS (2015) The role of metamorphic fluids in the formation of ore deposits. In: Jenkin GRT, Lusty PAJ, McDonald I et al (eds) Ore deposits in an evolving earth. Geological Society, London, pp 117–134

Yund RA, Snow E (1989) Effects of hydrogen fugacity and confining pressure on the interdiffusion rate of NaSi-CaAl in plagioclase. J Geophy r: Solid Earth 94(B8):10662–10668. https://doi.org/10.1029/jb094ib08p10662

Zhang Y (2008) Geochemical Kinetics, Princeton University Press, ISBN: 978069112432.